A Three-Stage-Concatenated Non-Linear MMSE Interference Rejection Combining Aided MIMO-OFDM Receiver and its EXIT-Chart Analysis

Jue Chen, Siyao Lu, Member, IEEE, Tsang-Yi Wang, *Member, IEEE*, Jwo-Yuh Wu, *Member, IEEE*, Chih-Peng Li, *Fellow, IEEE*, Soon Xin Ng, *Senior Member, IEEE*, Robert G. Maunder, *Senior Member, IEEE* and Lajos Hanzo, *Life Fellow, IEEE*

Abstract—The demodulation reference signal of the 5G Multiple-Input Multiple-Output Orthogonal Frequency-Division Multiplexing (MIMO-OFDM) waveform has been designed for supporting Minimum Mean-Square Error-Interference Rejection Combining (MMSE-IRC) equalization, which has become the state-of-the-art, owing to its enhanced performance in the case of dense frequency reuse, which is typical in 5G. By contrast, in the 4G LTE system, typically turbo equalization techniques were used. The family of Non-Linear receiver techniques tend to be eminently suitable for tough rank-deficient scenarios, when the received signal constellation becomes linearly non-separable. Hence, we propose a novel receiver for interference-constrained MIMO-OFDM systems, relying on a linear MMSE-IRC detector intrinsically amalgamated with an additional NL equalizer. In this way, we may achieve the best of both worlds, retaining the interference rejection capability of the MMSE-IRC detector and the superior performance of the NL equalizer. Our solution circumvents the potential failure of the MMSE-IRC, when the MIMO channels' degree freedom is completely exhausted by the desired users in case the transmitter has a high number of transmission layers for example. Based on this concept, we then design a novel NL equalizer relying on the Smart Ordering and Candidate Adding (SOCA) algorithm. This reduced complexity NL detection algorithm is particularly well suited for practical hardware implementation using parallel processing at a low latency. Briefly, the proposed scheme employs the MMSE-IRC detector for mitigating the interference. It makes the first estimate of the desired user signals and then uses the SOCA detector for further decontaminating the received signals. It also generates the soft information, enabling turbo equalization, wherein iterative detector and decoder iteratively exchange their soft information. We present BLock Error Rate (BLER) results, which show that the proposed scheme can always achieve superior performance to the conventional MMSE-IRC detector at the cost of increasing the complexity. In some cases, our proposed scheme can obtain about 1.5 dB gain, at the cost of 4 times higher complexity. We demonstrate that the complexity of the SOCA detector can be reduced by adjusting its parameterization or at the cost of reducing the self-consistency of the soft information produced by the SOCA detector, which slightly erodes the BLER performance. In order to mitigate this, we propose to use Deep Learning (DL) for enhancing the accuracy of the soft information. Using this technique, we show that the MMSE-IRC-NL-SOCA detector relying on DL attains about 3 dB gain at the cost of only marginally increasing the complexity, compared to the proposed MMSE-IRC-NL-SOCA scheme.

Index Terms—Interference rejection combining, smart ordering and candidate adding, deep learning, iterative detection and decoding, a MIMO-OFDM system

I. INTRODUCTION

In successive generations of wireless communication systems, higher and higher spectral efficiency and throughput have been targeted and this has led to the introduction of multi-user Multiple-Input and Multiple-Output Orthogonal Frequency-Division Multiplexing (MIMO-OFDM) [1], [2],which suffers from multi-user interference. Traditionally, the multi-user interference has been mitigated by careful beamforming and inter-cell interference reduction combined with sophisticated frequency reuse scheduling. However, these techniques are unable to completely eliminate the interference and the resultant residual interference degrades the performance. Meanwhile, there has been a flurry of recent activity in industrial standardisation bodies on uplink performance improvement techniques. In particular, the O-RAN alliance has completed a large amount studies [3], which have demonstrated that the uplink performance of a 5G cellular system is predetermined by its beamforming and MIMO capability. This investigation in [3] has considered both linear and Non-Linear (NL) techniques for equalisation, highlighting the importance of exploring new techniques and algorithms to improve the uplink performance. Motivated by this, interference suppression has recently become a pivotal research topic [4]–[13]. Minimum Mean Squared Error based Interference Rejection Combining (MMSE-IRC) has been proposed as a linear MIMO detection technique [4], for mitigating both the interference and noise. It has also been considered in the design of the 3GPP 5G new radio standard [14]. The correlation between the signals received by the different antennas can be used for identifying the interference and for separating it from the uncorrelated noise. Then the equalizer weights may be directly optimized for emphasizing the desired signal and for mitigating both the noise and the interference. Recent applications of the MMSE-IRC technique include Unmanned Aerial Vehicles (UAVs) [15], Non-Orthogonal Multiple Access (NOMA) [16], the Eigen domain [17] and partial Fast Fourier

Transform (FFT) based demodulation [18].

To elaborate further, the MMSE-IRC relies on a low-complexity linear algorithm, which treats interference as a stationary Gaussian process and employs a linear equalizer [4], [19]. However, in line with other linear algorithms, the MMSE-IRC has limited performance, particularly when the received signal constellation becomes linearly non-separable, or when the interference is not a stationary Gaussian process. In particular, the linear MMSE-IRC detector exhibits poor performance, when all the degrees of freedom provided by the MIMO channel are exhausted by the desired users [17]. More specifically, this will occur when the number of layers of the desired users is equal to the number of receiver antennas, for example. Upon exceeding this limit, the received signal constellation tends to become linearly non-separable and hence linear receivers fail to separate them, which results in a high residual BLock Error Rate (BLER), to a remedy, NL receivers may be harnessed for achieving improved performance. However, employing a NL technique such as the Maximum Likelihood (ML) equalizer operating in the presence of interference tends to have excessive complexity, since all the combinations of signals transmitted both by the interfering users and the desired users have to be considered. Furthermore, in order to apply NL algorithms for MIMO detection in the presence of interference, prior information about the interference, such as the choice of the modulation scheme, the number of layers, and the channel gains of the interfering users may be required. This is often impractical. On the other hand, if the NL algorithms ignore the interference and treat it as noise, then the performance may become even worse than that achieved by MMSE-IRC.

Given this motivation, we achieve the best of both worlds by efficient interference mitigation at a low complexity with the aid of MMSE-IRC detection, as well as high-performance NL detection. We achieve this by reformulating the MMSE-IRC detector for ensuring that its outputs become compatible with a serially concatenated NL detector. More specifically, we modify the outputs of the linear MMSE-IRC, so that it provides the specific tailor-made inputs required a the NL detector. In this way, the linear MMSE-IRC detector obtains the first estimated signal for the desired user, and then a serially concatenated NL detector is employed for recovering the desired signal. In this way, our proposed technique attains a good performance even when the desired user exploits all degrees of freedom provided by the MIMO channel, and when the MMSE-IRC detector would fail to mitigate the interference and detect the desired signals.

In a traditional NL MIMO receiver, the inputs of a NL MIMO detector are constituted by the received signal, the channel state information, and the noise variance. Hence, we improve the MMSE-IRC detector to provide not only an equalized version of both the received signal but also an equivalent equalized version of the channel state information and of the covariance matrix.

Having introduced this novel concept, we then conceive a specific implementation, wherein the proposed improvement of the MMSE-IRC detector is combined with a NL Smart Ordering Aided Candidate Adding (NL-SOCA) [20] detector,

which has a practical implementation compellingly a low complexity. Since the MMSE-IRC detector rejects interference, there is no need for the NL-SOCA to consider interference during the detection process. Furthermore, a DL-aided LLR correction technique [21] is conceived for further improving the performance.

We explicitly contrast our contributions to the state-of-the-art in Table I and detail them below:

TABLE I
CONTRASTING OUR CONTRIBUTION TO THE STATE-OF-THE-ART

	[7]	[8]	[9]	[10]	[11]	[12]	[13]	This work
MMSE-IRC	√	√	√	√	√	√	√	√
Deep learning		√						√
Throughput improvement			√	√	√			√
MIMO-OFDM	√	√	√			√	√	√
Iterative receiver					√	√	√	√
NL detector								√
EXIT chart analysis								√

- We propose a concept that combines a linear detector with a low-complexity NL detector for mitigating the hostile multi-user interference encountered in MIMO-OFDM system. This concept is designed for retaining both the low-complexity interference rejection capability of the linear MMSE-IRC detector, as well as the high performance of a non-linear MIMO detector. We realize this concept by further developing the linear MMSE-IRC detector for making it compatible with a serially concatenated non-linear algorithm in support of MIMO detection in the presence of interference. More specifically, we formulate the outputs of the linear MMSE-IRC detector for appropriately conditioning the inputs required by a serially concatenated non-linear detector. This concept is designed for retaining both the low-complexity interference rejection capability of the linear MMSE-IRC detector, as well as the high performance of a non-linear MIMO detector.

- The compelling amalgam of the linear MMSE-IRC detector with the NL-SOCA detector is then intrinsically integrated with a MIMO-OFDM system operating in the presence of interference. Here, the linear MMSE-IRC detector is used for mitigating the inference and outputting a first estimate. Then the NL-SOCA detector considers various possible combinations of the desired signals in order to identify the most likely one. The proposed technique is shown to consistently outperform the stand-above MMSE-IRC detector. In particular, we demonstrate that in some cases where the conventional MMSE-IRC detector fails to recover the transmitted signals of the desired user, the proposed MMSE-IRC-NL-SOCA scheme still maintains a good performance. Otherwise, in situations where the conventional MMSE-IRC detector succeeds in achieving good decoding performance, the proposed MMSE-IRC-NL-SOCA scheme can still achieve around 1.5 dB gain, at the cost of increasing the complexity by a factor of four.

- We demonstrate that an additional DL-aided Logarithmic-Likelihood Ratio (LLR) correction algorithm may be

harnessed for beneficially adjusting the output of the NL detector in order to make it more self-consistent. We show that this improves the decoding performance, especially when a low-complexity NL algorithm is adopted, such as the NL-SOCA detector. We show that in the case of using a high coding rate and a high Signal-to-Interference Ratio (SIR), the DL-aided LLR correction module improves the performance of the proposed MMSE-IRC-NL-SOCA scheme by about 3 dB, at the cost of only increasing the complexity by 2%.

- We provide the semi-analytic EXtrinsic Information Transfer (EXIT) chart analysis of our iterative receiver relying on the proposed MMSE-IRC-NL-SOCA scheme and the 5G 3GPP Low-Density Parity Check (LDPC) decoder. In particular, this EXIT chart analysis unveils, why the DL-aided LLR correction scheme improves the performance.

The rest of this paper is organized as follows. Section II introduces our novel MMSE-IRC detector designed for concatenation with a NL detector. Then, in Section III we conceive a beneficial instantiation of the proposed technique, namely the LDPC-coded MMSE-IRC-NL-SOCA scheme advocated, which is intrinsically integrated with MIMO-OFDM operating in the presence of interference, relying on our proposed DL-aided LLR correction scheme. Section IV quantifies the complexity of this LDPC-coded MMSE-IRC-NL-SOCA scheme. We provide EXIT charts for analyzing the proposed MMSE-IRC-NL-SOCA system in Section V. Our simulation results are presented in Section VI, while our conclusions are offered in Section VII.

II. Modified MMSE-IRC detector designed for concatenation with a NL detector

In this section, we introduce our novel concept of reformulating the MMSE-IRC detector, in order to facilitate its concatenation with a Soft-input Soft-output (SISO) NL detector.

Fig. 1 presents the block diagram of a system comprising MIMO transmitters for a desired user and an interfering user, as well as a MIMO receiver. The transmitter of both the desired and of the interfering user comprises a channel encoder, interleaver, QAM modulator, and an 'RF' transmit module. Here, the radio transmitter includes the OFDM and 'RF' chain components. Following transmission over a MIMO channel, both the desired signals $\mathbf{X}_1$, and the interference $\mathbf{X}_2$ transmitted by the interfering user reach the receiver. The 'RF' receiver module performs the inverse operations. In practice, the received signal $\mathbf{Y}$ may include some pilot symbols, which are processed by the channel estimator for estimating the channel matrix, the SIR σ_i^2 and the noise variance σ_n^2. Then, as described in Section II-A, the MMSE-IRC detector firstly processes the interference-infested received signals $\mathbf{Y}$ in order to mitigate the interference and obtain a first estimate of the desired signal $\hat{\mathbf{X}}_1$, an equivalent channel matrix $\mathbf{H}_e$, and a covariance matrix $\mathbf{R}_u$. Following this, as described in Section II-B, these are entered into the SISO NL detector, which exchanges soft information with the channel decoder in several

iterations, in order to obtain the final estimated desired signal $\hat{\boldsymbol{a}}_1$.

In order to elaborate on the details a little further, let us consider the desired user's transmitter. The desired user's information bit vector $\boldsymbol{a}_1$ comprises K' number of bits and it is encoded by a channel encoder, in order to obtain the encoded bit vector $\boldsymbol{b}_1$, which comprises E number of bits. Hence the coding rate is $R = K'/E$ [1]. Following this, the order of the encoded bits in the vector $\boldsymbol{b}_1$ is pseudo-randomly rearranged by the interleaver Π of Fig. 1, in order to obtain the E-bit vector $\boldsymbol{c}_1$, whose bits are QAM modulated and distributed across the N_u number of transmitter antennas by the modulator, in order to obtain the desired user's signal $\mathbf{X}_1 \in \mathcal{C}^{N_u \times F}$. Here, $G = 2^m$-ary QAM modulation is employed, so that m bits are transmitted per symbol, and $F = E/(mN_u)$ is the number of time or frequency elements occupied by the transmitted signal depending on whether or not OFDM modulation is used. More specifically, each antenna of Fig. 1 transmits a sequence comprising F QAM symbols, over a series of F time or frequency elements. Each element of the signals $\boldsymbol{x}_1[t]$ is transmitted in the tth time or frequency resource with an average power of E_s, where $\boldsymbol{x}_1[t]$ is the tth column of $\mathbf{X}_1$. Then, the modulated symbols are passed to the 'RF' transmitter module, in order to obtain $\mathbf{S}_1$ before transmission, as seen in Fig. 1.

Following transmission over the MIMO channel, the 'RF' receiver block performs the inverse operations of the 'RF' transmitter block of the desired and interfering users, and hence the received signals in the $t^{th}, t \in [1, F]$ time or frequency resource slot may be expressed as

$$\boldsymbol{y}[t] = \mathbf{H}_1[t]\boldsymbol{x}_1[t] + \frac{1}{\sqrt{\sigma_i^2}}\mathbf{H}_2[t]\boldsymbol{x}_2[t] + \boldsymbol{n}[t]$$
$$= \mathbf{H}_1[t]\boldsymbol{x}_1[t] + \boldsymbol{v}[t]. \qquad (1)$$

Here, we use the notation N_u to represent the number of Transmit Antennas (TAs) employed by the desired user, N_i is the number of TAs employed by the interfering user and N_r is the number of the Receive Antennas (RAs). In the tth time or frequency resource element, $\boldsymbol{x}_1[t] \in \mathbb{C}^{N_u \times 1}$ is the signal vector transmitted from the desired user, while $\boldsymbol{x}_2[t] \in \mathbb{C}^{N_i \times 1}$ is the signal vector transmitted from the interfering user. Furthermore, $\boldsymbol{y}[t] \in \mathbb{C}^{N_r \times 1}$ is the signal received in the tth time or frequency element and provides the tth column of $\mathbf{Y}$. Here, $\mathbf{H}_1[t] \in \mathbb{C}^{N_r \times N_u}$ is the channel matrix between the desired user and the receiver, which has unit power. Likewise, $\mathbf{H}_2[t] \in \mathbb{C}^{N_r \times N_i}$ is the channel matrix between the interfering user and the receiver, which has unit power. Furthermore, σ_i^2 represents the SIR, while $\boldsymbol{n} \in \mathbb{C}^{N_r \times 1}$ is a zero-mean complex Gaussian distributed random noise vector, where each element has a variance of σ_n^2.

Upon receiving the signal $\boldsymbol{y}[t]$, the channel estimator provides an estimate of both the channel matrix $\mathbf{H}_1[t]$ as well as of the covariance matrix $\mathbf{R}_v[t] \in \mathbb{C}^{N_u \times N_u}$, which may be obtained based on pilot symbols that are multiplexed with

---

[1]In SectioNn III, we will adopt the 3GPP LDPC channel encoder, hence here we use the notations K' and E in alignment with the notations used by 3GPP for the input and output of the LDPC encoder.
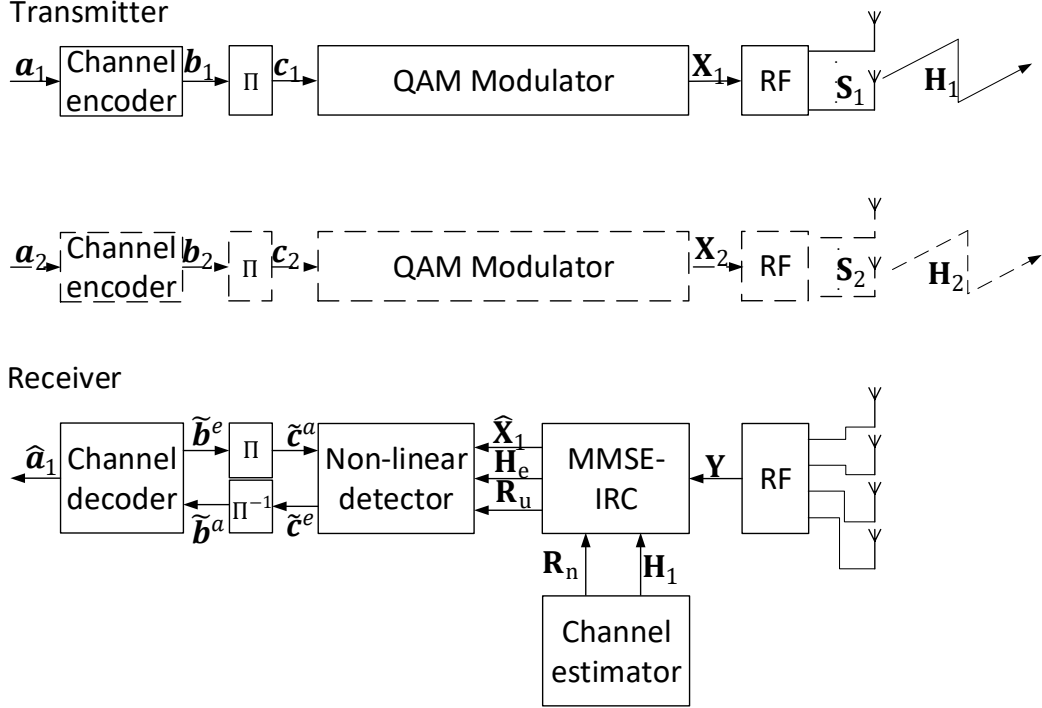
Fig. 1. The schematic of a system contaminated by an interfering user, where the receiver combines the MMSE-IRC with a NL detector.

$\boldsymbol{y}[t]$ [19]. The estimate of the channel matrix $\mathbf{H}_1[t]$ and of the covariance matrix $\mathbf{R}_v[t]$ are then forwarded to the MMSE-IRC detector of Fig. 1, alongside the received signal $\boldsymbol{y}[t]$. Following this, the linear MMSE-IRC detector is activated for mitigating the interference and obtains a first estimate of the desired signal $\hat{\boldsymbol{x}}_1[t] \in \mathbb{C}^{N_u \times 1}$ in each of the F time or frequency element. Then, the first estimate of the desired user $\hat{\boldsymbol{x}}_1[t]$ is entered into the NL detector of Fig. 1, which is harnessed for further iterative detection and decoding. Furthermore, the NL detector may also be provided with a reformulated equivalent channel matrix $\mathbf{H}_e[t] \in \mathbb{C}^{N_u \times N_u}$ and a corresponding covariance matrix $\mathbf{R}_u[t] \in \mathbb{C}^{N_u \times N_u}$ in each of the F time or frequency element, which are obtained by the MMSE-IRC detectors as detailed later in Section II-A. The NL detector of Fig. 1 generates a vector $\tilde{c}^e$ of *extrinsic* LLRs, which initiates an iterative detection and decoding process. Here, the *extrinsic* LLR vector $\tilde{c}^e$ comprises $E = K'/R$ LLRs, which are derived from the signals received across all F time or frequency elements, as detailed in Section II-B. The order of the *extrinsic* LLRs in vector $\tilde{c}^e$ is rearranged by the de-interleaver Π^{-1} of Fig. 1, which has the inverse action of the interleaver Π adopted in the desired user's transmitter. Following this, the resultant *a priori* LLR vector $\tilde{b}^a$ is forwarded to the channel decoder of Fig. 1 [22], which generates the *extrinsic* LLRs $\tilde{b}^e$ in response. The order of the *extrinsic* LLRs in the vector $\tilde{b}^e$ is rearranged by an interleaver Π in order to generate the *a priori* LLR vector $\tilde{c}^a$, which is then entered into the NL detector of Fig. 1. This may be used for initiating a second iteration in which the information

provided by the *a priori* LLR vector $\tilde{b}^e$ is combined with the information gleaned from the first estimated signal $\hat{\mathbf{X}}_1$, in order to obtain the improved *extrinsic* LLR vector $\tilde{c}^e$ of Fig. 1. After I_{outer} iterations between the NL detector and channel decoder, the latter may make a final decision and outputs an estimated binary signal $\hat{a}_1$ corresponding to the desired user. Let us now detail the internal operations of the modified linear MMSE-IRC detector of Fig. 1 in Section II-A and of the NL detector in Section II-B.

A. A linear MMSE-IRC detector

In this section, we detail our MMSE-IRC detector, which is designed for mitigating the interference in the received signal and for generating the inputs that are required for the NL detector. More specifically, the inputs of a conventional SISO NL detector comprise the received signal, an estimated channel matrix, and an estimated covariance matrix [23]. In our proposed concatenation of the MMSE-IRC detector with a NL detector, the first estimate of the desired user signals $\hat{\boldsymbol{x}}_1[t]$ provided by the MMSE-IRC detector fulfills the role of the received signal considered by the NL detector in the tth time or frequency element. More specifically, this first estimate of the desired user signal may be expressed as

$$\hat{\boldsymbol{x}}_1[t] = \mathbf{H}_e[t]\boldsymbol{x}_1[t] + \boldsymbol{u}[t], \qquad (2)$$

where $\mathbf{H}_e[t]$ is an equivalent channel matrix in the tth time or frequency element. Furthermore, $\boldsymbol{u}[t]$ represents the noise in the tth time or frequency element, which may include both Gaussian noise and the residual interference was not

completely cleaned up by the MMSE-IRC detector. This noise may be characterized by a covariance matrix that is formulated as $\mathbf{R}_{\mathrm{u}}[t] = E(|\boldsymbol{u}[t]\boldsymbol{u}[t]^H|^2)$.

The first estimate of the desired user signal in the tth time or frequency element shown as Eq. (2) may be derived from Eq. (3) [19]:

$$\hat{\boldsymbol{x}}_1[t] = \mathbf{W}_{\mathrm{MMSE-IRC}}[t]\boldsymbol{y}[t] \tag{3}$$

Here, $\mathbf{W}_{\mathrm{MMSE-IRC}}[t] \in \mathbb{C}^{N_{\mathrm{u}} \times N_{\mathrm{u}}}$ is a weight matrix employed for calculating the first estimate of the desired user signal $\hat{\boldsymbol{x}}_1[t]$ in the tth time or frequency element.

According to Eq. (1), $\boldsymbol{y}[t]$ may be substituted into Eq. (3) and expanded to obtain Eq. (4), shown below:

With reference to Eq. (2), we have $\mathbf{H}_{\mathrm{e}}[t] = \mathbf{W}_{\mathrm{MMSE-IRC}}[t]\mathbf{H}_1[t]$ and $\boldsymbol{u}[t] = \mathbf{W}_{\mathrm{MMSE-IRC}}[t](\sigma_{\mathrm{i}}^2\mathbf{H}_2[t]\boldsymbol{x}_2[t] + \boldsymbol{n}[t])$. In a practical case, the channel information of the desired user $\mathbf{H}_1[t]$ may be estimated by the channel estimator based on the pilot symbols transmitted by the desired user [19]. However, in this case, the channel information of the interfering user $\mathbf{H}_2[t]$ may be unknown to the receiver. In this case, the weighting matrix may be expressed as

$$\mathbf{W}_{\mathrm{MMSE-IRC}}[t] = \mathbf{H}_1^H[t](\mathbf{H}_1[t]\mathbf{H}_1^H[t] + \mathbf{R}_{\mathrm{v}}[t])^{-1}. \tag{5}$$

Here, the covariance matrix $\mathbf{R}_{\mathrm{v}}[t]$ of both the noise and of the interference in Eq. (1) is calculated by the channel estimator using the received pilot symbols and the estimated channel information $\mathbf{H}_1[t]$ of the desired user, as detailed in [19]. More specifically, the covariance matrix $\mathbf{R}_{\mathrm{v}}[t]$ may be calculated by exploiting the knowledge of the pilot symbols $\boldsymbol{x}_1[t]$ transmitted by the desired user and the channel state information $\mathbf{H}_1[t]$ obtained using channel estimation for the desired user. This is formulated as:

$$\mathbf{R}_{\mathrm{v}}[t] = (\boldsymbol{y}[t] - \mathbf{H}_1[t]\boldsymbol{x}_1[t])(\boldsymbol{y}[t] - \mathbf{H}_1[t]\boldsymbol{x}_1[t])^H. \tag{6}$$

Here $(\boldsymbol{y}[t] - \mathbf{H}_1[t]\boldsymbol{x}_1[t])$ represents a noise plus interference signal, since the pilot symbols of the desired user have been subtracted.

In order to imitate this practical technique for obtaining the covariance matrix $\mathbf{R}_{\mathrm{v}}[t]$, we assume perfect knowledge of the desired user and the noise plus interference signal $(\boldsymbol{y}[t] - \mathbf{H}_1[t]\boldsymbol{x}_1[t])$.

Otherwise, in an idealistic case, the channel state information of both the desired user $\mathbf{H}_1[t]$ and of the interfering user $\mathbf{H}_2[t]$ is assumed as prior knowledge at the receiver. In this case, the weighting matrix of the MMSE-IRC in the tth time or frequency element is given by [19]

$$\begin{aligned}\mathbf{W}_{\mathrm{MMSE-IRC}}[t] &= \mathbf{H}_1^H[t](\mathbf{H}_1[t]\mathbf{H}_1^H[t] + \mathbf{R}_{\mathrm{v}}[t])^{-1} \\ &= \mathbf{H}_1^H[t](\mathbf{H}_1[t]\mathbf{H}_1^H[t] + \sigma_{\mathrm{i}}^2\mathbf{H}_2[t]\mathbf{H}_2^H[t] + \sigma_{\mathrm{n}}^2\mathbf{I})^{-1}. \end{aligned} \tag{7}$$

Furthermore, in the idealistic case, the noise covariance matrix of Eq. (2) is expressed as

$$\begin{aligned}\mathbf{R}_{\mathrm{u}}[t] &= E(|\boldsymbol{u}[t]\boldsymbol{u}[t]^H|^2) \\ &= \sigma_{\mathrm{i}}^2(\mathbf{W}_{\mathrm{MMSE-IRC}}[t]\mathbf{H}_2[t] \times (\mathbf{W}_{\mathrm{MMSE-IRC}}[t]\mathbf{H}_2[t])^H) \\ &\quad + \sigma_{\mathrm{n}}^2\mathbf{W}_{\mathrm{MMSE-IRC}}[t]\mathbf{W}_{\mathrm{MMSE-IRC}}[t]^H. \end{aligned} \tag{8}$$

Here, each diagonal element of the covariance matrix $\mathbf{R}_{\mathrm{u}}[t]$ represents the noise variance corresponding to each element of the desired user's signal $\boldsymbol{x}_1[t]$. Here, we adopt the notation $\boldsymbol{P}[t] = diag(\mathbf{R}_{\mathrm{u}}[t])$ to denote the diagonal elements of the covariance matrix $\mathbf{R}_{\mathrm{u}}[t]$.

Fig. 2 presents results based on a pair of assumptions. The first plot in Fig. 2 considers the assumption of having perfect channel state information for both the interfering and desired user, labelled as 'MMSE-IRC, perfect CSI for both the interfering and desired user'. The second plot in Fig. 2 considers the assumption of perfect channel state information for the desired user and perfect knowledge of the noise plus interference, labelled as 'MMSE-IRC, perfect CSI for the desired user and perfect knowledge of the noise plus interference'. These results show that the assumption of perfect knowledge of the interference plus noise signal offers superior results. This may be explained by the observation that the assumption of having perfect knowledge of the interfering user's channel information only provides statistical knowledge of the interfering user's channel, without having the instantaneous knowledge of what the interference plus noise truly is, which is employed in the case of the perfect knowledge of the interference plus noise. In practice, the accuracy of the interference plus noise signal obtained in the receiver will be influenced by how well the desired user's channel information may be estimated, according to Eq. (6). While the assumption that we do not have perfect knowledge of the interfering user's channel state information is the only valid option in realistic scenarios, we adopt this assumption throughout the remainder of this paper, since the results obtained by having perfect knowledge of the interference plus noise signal are optimistic. Here, Eqs. ((3), (7), (8)) are used in our simulations.

B. The concatenated NL detector

For a soft-output NL detector operating in the absence of interference, where the received signal in the tth resource element is given by $\boldsymbol{y}[t] = \mathbf{H}_1[t]\boldsymbol{x}_1[t] + \boldsymbol{n}[t]$, each of the LLRs derived from the tth resource element is calculated as follows after the application of Bayes' rule, the max-log approximation, and with the aid of the *a priori* information provided by the channel decoder [20], shown as Eq. (9):

Here $\mathcal{X}_j^0$ denotes the sub-set of all candidates in the set $\mathcal{X}$, in which the encoded bit sequence $\hat{\boldsymbol{c}}$ has the value 0 assigned to the corresponding bit $\hat{c}_j$. Similarly, $\mathcal{X}_j^1$ denotes the set of all candidates for the encoded bit sequence $\hat{\boldsymbol{c}}$ that has the value 1 assigned to the corresponding bit $\hat{c}_j$. Here, j is in the range from 1 to $N_{\mathrm{u}}m$, since there are N_{u} QAM-based IQ symbols transmitted in each resource element and each QAM symbol conveys m bits.

However, in a system subject to interference, the received signal $\boldsymbol{y}$ is influenced by the interference and may not generate accurate *extrinsic* LLRs corresponding to the bit sequence $\boldsymbol{c}_1$ of the desired user for the channel decoder, unless first MMSE-IRC is employed for mitigating the interference. Here, in the proposed scheme of Fig. 1, the NL detector takes its input from the serially concatenated MMSE-IRC detector. Hence with reference to Eq. (2), Eq. (9) is reformulated to Eq. (10):

$$\hat{\boldsymbol{x}}_1[t] = \mathbf{W}_{\mathrm{MMSE-IRC}}[t] \left(\mathbf{H}_1[t]\boldsymbol{x}_1[t] + \frac{1}{\sqrt{\sigma_{\mathrm{i}}^2}}\mathbf{H}_2[t]\boldsymbol{x}_2[t] + \boldsymbol{n}[t] \right)$$

$$= \mathbf{W}_{\mathrm{MMSE-IRC}}[t]\mathbf{H}_1[t]\boldsymbol{x}_1[t] + \mathbf{W}_{\mathrm{MMSE-IRC}}[t] \left(\sigma_{\mathrm{i}}^2\mathbf{H}_2[t]\boldsymbol{x}_2[t] + \boldsymbol{n}[t] \right). \tag{4}$$
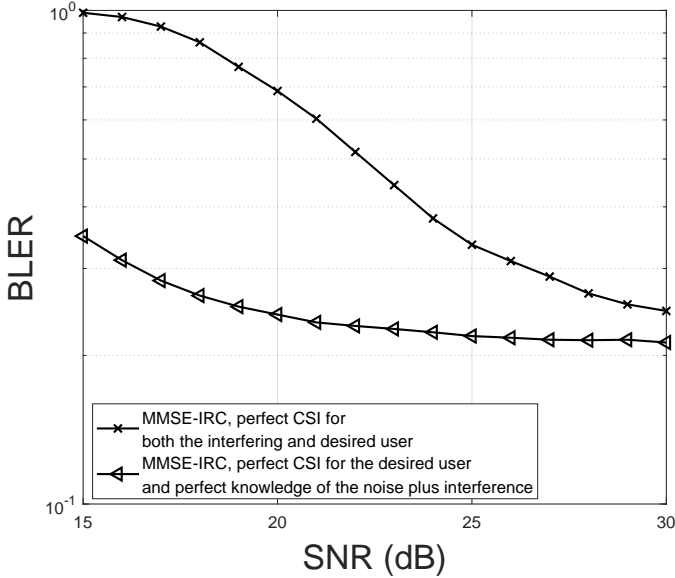
Fig. 2. Comparison between the assumption of perfect channel state information for both the interfering and desired users, with the assumption of perfect knowledge of the interference plus noise signal for the case of $N_{\mathrm{r}} = 4$ RAs, $N_{\mathrm{u}} = 4$ user TAs, $N_{\mathrm{i}} = 1$ interfering user TA, $K' = 2048$ information bits, $L_{\max} = 4$ slicing value, coding rate $R = 1/2$, SIR $= 10$ dB, BG $= 2$, $N_{\mathrm{c}} = 64$ subcarriers, when using 16-QAM modulation for communication over a frequency selective fading channel with $L = 4$ channel taps.

Here, the outputs $\hat{\boldsymbol{x}}_1[t]$, $\mathbf{H}_{\mathrm{e}}[t]$ and $\boldsymbol{P}[t]$ gleaned from the MMSE-IRC detector replace $\boldsymbol{y}[t]$, $\mathbf{H}_1[t]$ and σ_{n}^2 in Eq. (9). Moreover, $\lceil \cdot \rceil$ represents the ceiling function.

The optimal NL MIMO detector relying on maximizing the likelihood objective function is the ML detection technique, which considers all legitimate candidates for the signal received from the desired user. However, the complexity of the ML algorithm may be high, when the number of TAs N_{u} or the modulation order m is high. For example, if $N_{\mathrm{u}} = 4$ and 16-QAM modulation is employed, the number of all possible combinations of the transmitted signals in each of the F resource elements is $16^4 = 65\,536$. Hence, a reduced-complexity NL MIMO detector may be preferred in practice. This will be explored in Section III, where we will introduce a particular parameterization of the proposed scheme.

III. LDPC-CODED MMSE-IRC-NL-SOCA SYSTEM MODEL

In this section, the novel LDPC-coded MMSE-IRC-NL-SOCA scheme of Figure. 3 is introduced. The channel decoder of the proposed system may indeed be changed to any SISO channel decoder. The 3GPP LDPC decoder is employed in this paper as a benefit of its powerful error correction capability. It is employed in 5G. Section III-A describes the transmitter,

which is used for both the desired user and the interfering user in our system simulations. Section III-B describes the channel model considered in our system simulations. In Section III-C, the proposed LDPC-coded MMSE-IRC-NL-SOCA scheme employing iterative detection and decoding is detailed.

A. Transmitter

In this section, we detail the specific scheme of Fig. 3, which employs the 3GPP LDPC encoder 3GPP [14] for channel encoding. This converts a K'-bit sequence $\boldsymbol{a}_1$ into an E-bit encoded sequence $\boldsymbol{b}_1$, in the case of the desired user. The specific order of the E bits in the sequence $\boldsymbol{b}_1$ is rearranged by the interleaver Π of Figure. 3, in order to generate the E-bit interleaved sequence $\boldsymbol{c}_1$. Furthermore, we employ a QAM modulator having the constellation set $\mathcal{A}$ of size $|\mathcal{A}|$, which maps the bits of the sequence $\boldsymbol{b}_1$ into IQ symbols for transmission over the N_{u} TAs, obtaining the parallel spatial streams $\mathbf{X}_1 \in \mathbb{C}^{N_{\mathrm{u}} \times F}$. The OFDM modulator of Fig. 3 decomposes the F signal symbols of $\mathbf{X}_1$ into N_b OFDM blocks, each having dimensions of $N_{\mathrm{u}} \times N_{\mathrm{c}}$, where each OFDM block contains $N_{\mathrm{c}} = F/N_b$ symbols. Then, each of the N_{u} rows in each OFDM block is transformed by an N_{c}-point Inverse Fast Fourier Transform (IFFT), which is extended by a Cyclic Prefix (CP) in order to obtain the transmitted signal $\mathbf{S}_1$ [24]. The signal $\mathbf{S}_1$ comprises N_b OFDM symbols for each of the N_{u} TAs. The procedures of the interfering user's transmitter are the same as the one of the desired user.

B. Channel

In this section, we detail the channel model to be harnessed both in Section III-C and in our system simulations in the later sections.

In this specific example, a frequency-selective fading channel is employed as a special case of the Rayleigh fading channel introduced in Section II. Here, the channel between the ith, $i = [1, \ldots, N_{\mathrm{u}}]$ TA and the jth, $i = [1, \ldots, N_{\mathrm{r}}]$ RA is parameterized by $\boldsymbol{\gamma}^{ji} = [\gamma_1^{ji}, \ldots, \gamma_l^{ji}, \ldots, \gamma_L^{ji}]^T$, where L is the number of the channel taps in the time domain. Here, each element γ_l^{ji} is generated as a complex Gaussian random variable with zero mean and variance σ_{s}^2. We assume that the elements γ_l^{ji} are independent and identically distributed (i.i.d.) and that the average energy of $\boldsymbol{\gamma}^{ji}$ is unity, so that, $E\left\{ \left\| \boldsymbol{\gamma}^{ji} \right\|^2 \right\} = 1$. Each element γ_l^{ji} remains constant throughout a frame consisting of N_b OFDM symbols and changes independently from frame to frame. Furthermore, perfect channel information of both the desired user and of the interfering user is assumed to be known at the receiver. The corresponding frequency domain fading channel of the kth, $k = [1, \ldots, N_{\mathrm{c}}]$ subcarrier may be expressed as $h^{ji}[k] = \sum_{l=1}^{L} \gamma_l^{ji} \exp(-2\pi\sqrt{-1}(l-1)(k-1)/N_{\mathrm{c}})$.

$$\tilde{c}^e(\hat{c}_j) \approx \left\{ \min_{\hat{\boldsymbol{x}}_1[t] \in \mathcal{X}_j^0} \frac{\|\boldsymbol{y}[t] - \mathbf{H}_1[t]\hat{\boldsymbol{x}}_1[t]\|^2}{\sigma_\mathrm{n}^2} - \frac{1}{2} \sum_{j=1}^{m \times N_\mathrm{u}} (2\hat{c}_j - 1) \times \tilde{c}^a(\hat{c}_j) \right\}$$
$$- \left\{ \min_{\hat{\boldsymbol{x}}_1 \in \mathcal{X}_j^1} \frac{\|\boldsymbol{y}[t] - \mathbf{H}_1[t]\hat{\boldsymbol{x}}_1\|^2}{\sigma_\mathrm{n}^2} - \frac{1}{2} \sum_{j=1}^{m \times N_\mathrm{u}} (2\hat{c}_j - 1) \times \tilde{c}^a(\hat{c}_j) \right\} - \tilde{c}^a(\hat{c}_j). \tag{9}$$

$$\tilde{c}^e(\hat{c}_{1j}) \approx \left\{ \min_{\hat{\boldsymbol{x}}_1[t] \in \mathcal{X}_j^0} \frac{\left\|\hat{\boldsymbol{x}}_1[t] - \mathbf{H}_\mathrm{e}[t]\hat{\hat{\boldsymbol{x}}}_1[t]\right\|^2}{P[t](\lceil \frac{j}{N_\mathrm{u}} \rceil)} - \frac{1}{2} \sum_{j=1}^{m \times N_\mathrm{u}} (2\hat{c}_{1j} - 1) \times \tilde{c}^a(\hat{c}_{1j}) \right\}$$
$$- \left\{ \min_{\hat{\boldsymbol{x}}_1[t] \in \mathcal{X}_j^1} \frac{\left\|\hat{\boldsymbol{x}}_1[t] - \mathbf{H}_\mathrm{e}[t]\hat{\hat{\boldsymbol{x}}}_1[t]\right\|^2}{P[t](\lceil \frac{j}{N_\mathrm{u}} \rceil)} - \frac{1}{2} \sum_{j=1}^{m \times N_\mathrm{u}} (2\hat{c}_{1j} - 1) \times \tilde{c}^a(\hat{c}_{1j}) \right\} - \tilde{c}^a(\hat{c}_{1j}). \tag{10}$$
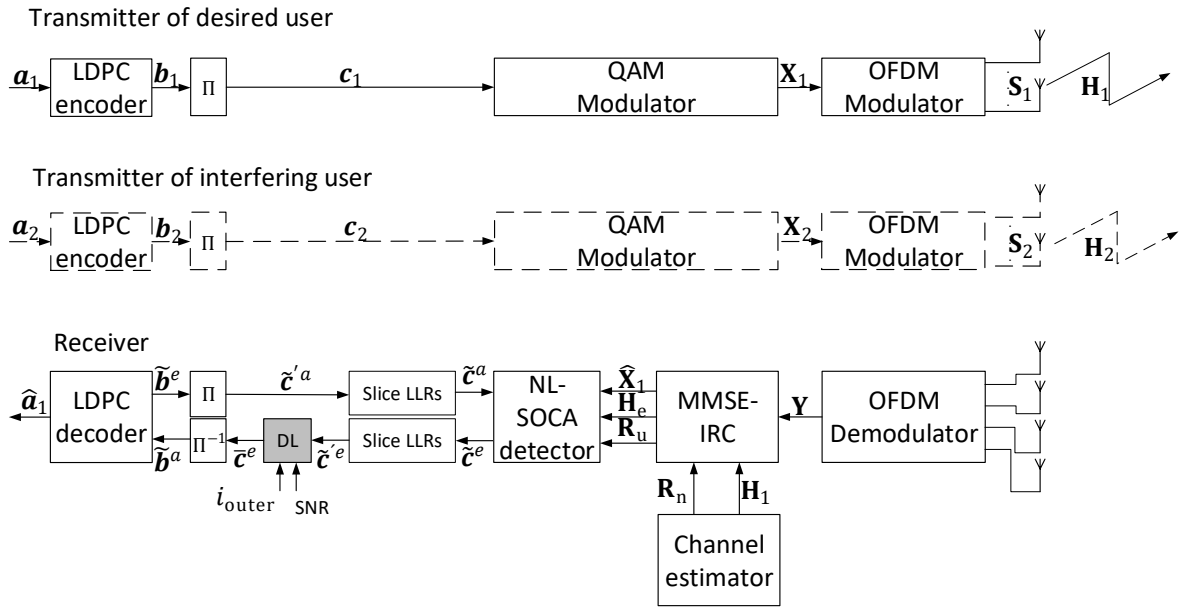

Fig. 3. Schematic of the transmitter and receiver for the proposed LDPC-coded MMSE-IRC-NL-SOCA/MMSE-IRC-NL-SOCA-DL scheme. The dashed lines correspond to interfering users and the grey-shaded block is specific to the MMSE-IRC-NL-SOCA-DL scheme.

C. Receiver

In this section, we continue by detailing the top-level operation of the receiver shown in Fig. 3, before delving into the internal operation of the NL-SOCA detector.

1) Top-level operation: The receiver of the proposed LDPC-coded MMSE-IRC-NL-SOCA scheme begins by OFDM demodulating each OFDM element received on each of the N_r RAs using an N_c-point FFT after removing the CP. In particular, the received signal $\mathbf{Y}$ obtained after OFDM demodulation is represented by Eq. (1), where $\mathbf{H}_1[t]$ and $\mathbf{H}_2[t]$ represent the frequency-selective channel between the desired user and the receiver, as well as between the interfering user and the receiver, respectively. Here, the received signal matrix $\mathbf{Y} \in \mathcal{C}^{N_\mathrm{r} \times F}$ comprises F resource elements for each of the N_r RAs.

As shown in Fig. 3, the received signal matrix $\boldsymbol{y}[t]$ is entered into the MMSE-IRC, which aims for mitigating the interference and outputs the first estimated signals $\hat{\boldsymbol{x}}_1[t]$ received from the desired user in each resource element using Eq. (2). Here, the MMSE-IRC detector is aided by the prior knowledge of the channel matrix, the noise variance σ_n^2, and the covariance matrix $\boldsymbol{R}_\mathrm{u}$ corresponding to each resource element. As mentioned in Section II, the MMSE-IRC detector outputs both the first estimated signal $\hat{\boldsymbol{x}}_1[t]$, as well as the equivalent channel matrix $\mathbf{H}_\mathrm{e}$ and the covariance matrix $\boldsymbol{R}_\mathrm{u}$, which are then forwarded to the NL-SOCA detector of Fig. 3. Then, the NL-SOCA detector processes the inputs provided by the MMSE-IRC detector and the vector $\tilde{\boldsymbol{c}}^a$ of E *a priori* LLRs provided by the LDPC decoder are then used for generating the E *extrinsic* LLRs $\tilde{\boldsymbol{c}}^e$. Note that during the first iteration

between the NL-SOCA detector and the LDPC decoder, all *a priori* LLRs in the vector $\tilde{c}^a$ are set to zeros.

Following detection, the *extrinsic* LLRs $\tilde{c}^e$ provided by the detector are then sliced in order to provide the LLR vector $\tilde{c}'$ and improve the decoding performance [25]–[27], shown in Fig. 3. More specifically, each element of the *extrinsic* LLR vector $\tilde{c}^e$ that is larger than the threshold $L_{\max}$ is set to $L_{\max}$, and each LLR that is smaller than $-L_{\max}$ is set to $-L_{\max}$. However, owing to the limited complexity of the NL-SOCA detector, the LLRs of the vector $\tilde{c}'^e$ may not be self-consistent, with some LLRs having exaggerated magnitudes representing over-confidence and some LLRs having unwarranted low magnitudes that express overly low confidence. In this case, the DL module of Fig. 3 may be trained and harnessed for correcting the *extrinsic* LLRs of the vector $\tilde{c}'^e$, in order to arrive at unbiased *extrinsic* LLRs $\bar{c}^e$. Here, a Deep Neural Network (DNN) comprising a dense fully connected NN [28] may be harnessed and trained for the DL module for correcting the *extrinsic* LLRs. In this case, the training data of the DNN may be generated using the lookup tables and linear interpolation techniques introduced in [23]. More specifically, the DNN takes three inputs, namely the sliced *extrinsic* LLR values $\tilde{c}'^e$ to be corrected, the channel's Signal-to-Noise Ratio (SNR), as well as the iteration index i_{outer} between the NL-SOCA detector and LDPC decoder. In this case, opted for hiring 3 hidden layers and each layer has 6 neural nodes in the trained DNN. It has been shown that the DL module employed is easy to train at a low complexity and it has advantages compared to other signal processing algorithms available for correcting inconsistent LLRs such as lookup tables, which have a higher memory requirement [21].

After correction by the DL module, the order of the corrected *extrinsic* LLRs in the vector $\bar{c}^e$ may be rearranged using the de-interleaver Π^{-1} of Fig. 3, which has the reverse pattern of the interleaver Π used in the transmitter. The resultant *extrinsic* LLRs $\bar{c}^e$ become the *a priori* LLRs $\tilde{b}$ of the LDPC decoder [29]. Following the operation of the LDPC decoder, the order of the E resultant *extrinsic* LLRs in the vector $\tilde{b}^e$ are rearranged using the interleaver Π of Fig. 3 in order to obtain the vector $\tilde{c}'^a$ of E *a priori* LLRs. However, before forwarding the *a priori* LLR vector $\tilde{c}'^a$ to the SOCA detector, its LLR are sliced to the range $-L_{\max}$ to $L_{\max}$ as described above, in order to obtain the sliced *a priori* LLR vector $\tilde{c}^a$, which may be forwarded to the NL-SOCA detector for the next iteration. More specifically, I_{outer} iterations may be carried out between the NL-SOCA detector and LDPC decoder, before the LDPC decoder outputs the final estimated bit vector $\hat{a}_1$ for the desired user.

2) NL-SOCA detector: This subsection aims for introducing the NL-SOCA detector module of Fig. 3 in detail. As mentioned in Section II, the optimal ML algorithm often used for NL MIMO detection suffers from excessive complexity. Hence, the proposed LDPC-coded MMSE-IRC-NL-SOCA scheme employs the reduced-complexity NL-SOCA algorithm for NL detection. The aim of the NL-SOCA detector is to identify the most likely combinations of transmitted signals using a tree search and then populating the set $\mathcal{X}$ of Eq. (10) using only these combinations for calculating the *extrinsic*

LLR vector $\tilde{c}^e$.

Fig. 4 characterizes an example of a detection tree [23] used in the NL-SOCA algorithm to identify the candidate set $\mathcal{X}$ to be considered for calculating the *extrinsic* LLR vector $\tilde{c}^e$. The first step of the NL-SOCA detector is to employ the Ordered QR (OQR) decomposition technique of [20] This calculates the SNR of each MIMO layer and ranks them in descending order. The MIMO layer having the highest SNR is then mapped onto the first layer of the tree and each MIMO layer having a successively lower SNR is mapped to the remaining successive layers of the tree in successive order. Then, a tree traversal is adopted to search for the most likely combinations of transmitted signals by calculating the associated node metrics [23] for each layer. Here, the number of tree nodes that can be extended from each parent node is given by the number $|\mathcal{A}|$ of QAM constellation points used and each tree node corresponds to a legitimate code word. In the ith layer, M_i child nodes having the best node metrics are extended from each parent node. Then, the counter-hypotheses of the best child node emerging from the same parent node in the ith layer are also considered, although this step may be skipped in the first layer. Following this, the number of survivor nodes that remain extended from the ith layer is limited to the K_i candidates having the best node metrics. In a special case, all extended tree nodes survive when $K_i = \infty$. Next, the survivor nodes in the ith layer become the set of parent nodes for the next layer.

To elaborate, let us detail the tree search using the example of Fig. 4. The number of layers in this example is $N_{\text{u}} = 2$ and there are 4 child nodes for each parent node in each layer corresponding to the $|\mathcal{A}| = 2^m = 4$ constellation points of the QPSK modulation employed in this example. In the first layer, the $M_1 = 3$ tree nodes having the best node metrics are extended and all $M_1 = 3$ extended tree nodes are retained, because we adopt $K_1 = \infty$. In the second layer, $M_2 = 2$ child nodes emerge from each parent node, and the best child node in the second layer is associated with the code word '0 0', as indicated in Fig. 4, using a diagonally filled circle. Hence, the $m = 2$ counter-hypotheses are '0 1' and '1 0', which are indicated by the filled circles in Fig. 4. Then, the $K_2 = 5$ child nodes having the best metrics are retained and become the 5 survivor nodes. These provide the 5 candidate combinations, which are captured in the columns of the set

$$\mathcal{X} = \begin{bmatrix} 0 & 0 & 0 & 0 & 1 \\ 0 & 0 & 1 & 1 & 0 \\ 0 & 1 & 0 & 1 & 1 \\ 0 & 0 & 0 & 0 & 0 \end{bmatrix}. \tag{11}$$

Following completion of this process, all candidate combinations selected by the detection tree are used to calculate the *extrinsic* LLR vector $\tilde{c}^e$ which is then forwarded to the 'slice LLRs' block of Fig. 3.

IV. COMPLEXITY ANALYSIS

In this section, we quantify the complexity of the proposed MMSE-IRC-NL-SOCA algorithm employed in the proposed scheme of Fig. 3. The complexity of the proposed MMSE-IRC-NL-SOCA, MMSE-IRC-NL-SOCA-DL,
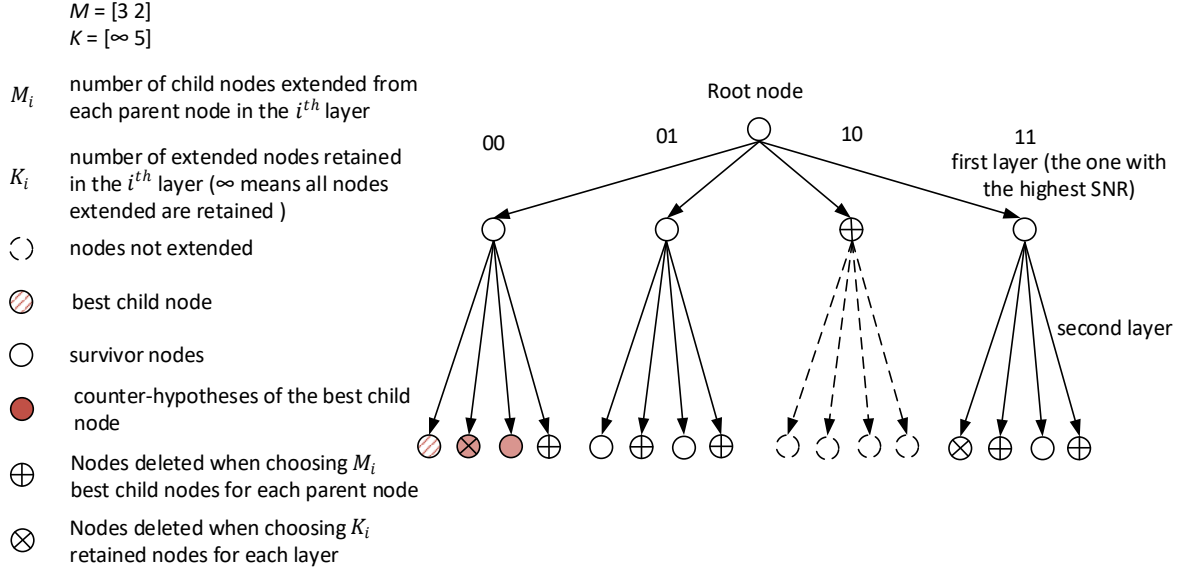
Fig. 4. An example of tree search in the NL-SOCA detector for the case $m = 2$ bits mapped into the QPSK modulated symbol transmitted in each of $N_{\mathrm{u}} = 2$ layers using $N_{\mathrm{u}} = 2$ transmit antennas.

and MMSE-IRC-DL schemes, as well as of a benchmarker MMSE-IRC scheme are quantified in terms of the number of different arithmetic operations performed in their various components. The overall complexity of each scheme is given by the sum of the different operations it employs.

In the MMSE-IRC benchmarker scheme, the outputs of MMSE-IRC module are processed by a demodulator, which outputs soft information. Subsequently, the soft information is passed to the LDPC decoder, which directly outputs the decoded bits, without performing any iterations with the demodulator. Building on this, the MMSE-IRC-DL scheme adopts a similar approach, but uses a DL module to correct the soft information produced by the demodulator before it is passed to the LDPC decoder. By contrast, in the MMSE-IRC-NL-SOCA scheme, the output of the MMSE-IRC module is processed by a NL-SOCA detector, which performs demodulation and passes soft information to the LDPC decoder. Furthermore, iterations are performed between the LDPC decoder and the NL-SOCA detector in the MMSE-IRC-NL-SOCA scheme. Building on this, the MMSE-IRC-NL-SOCA-DL scheme adopts a similar iterative approach, but with the difference that the soft information generated by the SOCA detector is corrected by a DL module before being passed to the LDPC decoder in each iteration.

Here, each scheme employs the 3GPP 5G LDPC code for channel decoding. The proposed MMSE-IRC-NL-SOCA scheme is an example of our proposed concatenation of MMSE-IRC with a NL detector, while the proposed MMSE-IRC-NL-SOCA-DL scheme additionally employs DL for correcting the *extrinsic* LLRs of $\tilde{c}'^e$. The transmitter of the LDPC-coded MMSE-IRC benchmarker is the same as that shown in Fig. 3 for the proposed scheme. However, the receiver of the benchmarker MMSE-IRC scheme is characterized as Fig. 5,

where the addition of DL results in the proposed MMSE-IRC-DL scheme. The benchmarker MMSE-IRC scheme employs the MMSE-IRC detector to obtain the estimated signals $\hat{x}_1$ arriving from the desired user. In contrast to the proposed MMSE-IRC-NL-SOCA scheme, the MMSE-IRC benchmarker uses soft demodulation [30] for calculating the *extrinsic* LLRs $\tilde{c}^e$, rather than using a NL detector. Then, the following components of the LDPC-coded MMSE-IRC benchmarker are similar to the proposed MMSE-IRC-NL-SOCA scheme discussed in Section III-C, except that no iterations are performed between the demodulator and the LDPC decoder. Furthermore, the DNN employed in the proposed MMSE-IRC-DL scheme employs only two hidden layers and each hidden layer has 4 neural nodes, since there is no iteration index as an input of this particular DNN and so a lower complexity can be used.

In the MMSE-IRC and NL-SOCA detector, we adopt the Householder's algorithm [31] for QR decomposition, and the LU decomposition [32] is used for matrix inversion. Each complex multiplication may be represented by four real-valued multiplications and two real-valued additions. Moreover, each complex addition may be considered to comprise two real-valued additions.

The number of operations required by the various schemes considered is quantified in Table II, for the case of transmitting $K' = 2048$ information bits, using an LDPC coding rate of $R = 1/2$, $I_{\mathrm{inner}} = 1$ iteration inside the LDPC decoder and $I_{\mathrm{outer}} = 1$ iteration performed between the NL-SOCA detector and LDPC decoder. If higher numbers of iterations are performed, the number of operations may be scaled up proportionately. Note that the MMSE-IRC scheme is only activated once, regardless of how many iterations are performed for the rest of the receiver and so the corresponding number of operations should not be scaled with the number of iterations.
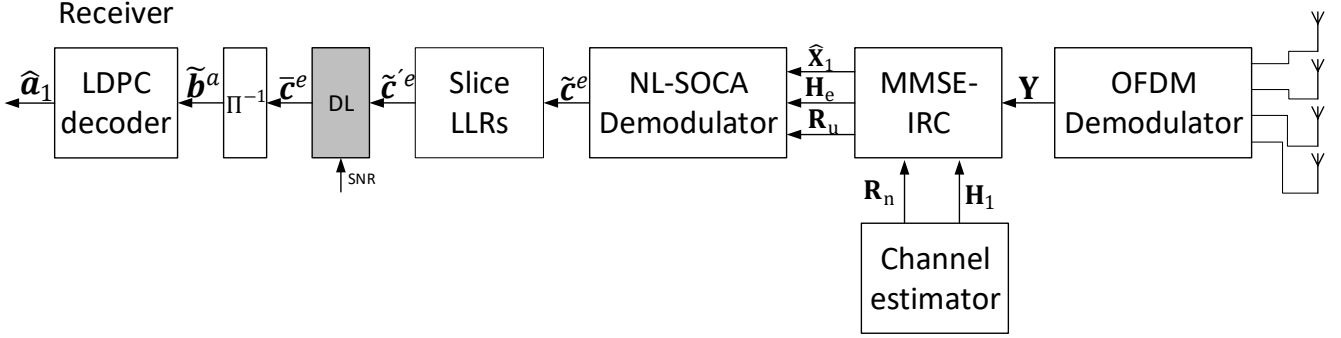
Fig. 5. Schematic of the receiver for the MMSE-IRC/MMSE-IRC-DL scheme. The grey shaded block is specific to the MMSE-IRC-DL scheme.

As discussed in Section III-C, the complexity of the DNN for DL in the proposed MMSE-IRC-NL-SOCA scheme is quantified for the case of using 3 hidden layers and each layer has 6 neural nodes.

V. EXIT CHART ANALYSIS OF THE ITERATIVE DETECTION AND DECODING PROCESSES

In this section, EXIT charts are employed for analyzing the iterative detection and decoding process exchanging soft *extrinsic* information between the NL-SOCA detector and the LDPC decoder of Fig. 4. They constitute powerful semi-analytic techniques, which visualize the iterative detection convergence and allow the design of near-capacity systems, as detailed in [33]. Briefly, the EXIT function of the LDPC decoder may be characterized by artificially generating *a priori* LLR vectors $\tilde{b}^a$, having different *a priori* Mutual Informations (MIs) I_{LDPC}^a in the range $[0, 1]$. These *a priori* LLR vectors may then be input to the LDPC decoder and the *extrinsic* MI I_{LDPC}^e of the *extrinsic* LLRs $\tilde{b}^e$ produced by the LDPC decoder may be measured. In this way, we may characterize and plot I_{LDPC}^e as a function of I_{LDPC}^a. Similarly, the EXIT function of the NL-SOCA detector may be characterized by generating *a priori* LLR vectors $\tilde{c}^a$ having different artificial *a priori* MIs $I_{\mathrm{NL-SOCA}}^a$ in the range $[0, 1]$. Together with the signal $\mathbf{Y}$ received over a simulated channel, these *a priori* LLRs may be entered into the MMSE-IRC detector and the NL-SOCA detector, respectively. Then, the *extrinsic* MI $I_{\mathrm{NL-SOCA}}^a$ of the sliced *extrinsic* LLRs $\tilde{c}'^e$ or the corrected *extrinsic* LLRs $\bar{c}^e$ generated by the NL-SOCA detector, slicing and DL may be measured. In this way, we may characterize and plot $I_{\mathrm{NL-SOCA}}^e$ as a function of $I_{\mathrm{NL-SOCA}}^a$. Since the *extrinsic* LLRs gleaned from one component become the *a priori* LLRs of the other during the iterative detection and decoding, we may invert the axes of the LDPC decoder, so that we have I_{LDPC}^a on the same axes as $I_{\mathrm{NL-SOCA}}^e$, and vice versa. We may then plot the LDPC EXIT function in the same figure as the NL-SOCA EXIT function, in order to create an EXIT chart as shown in Fig. 6 and 7.

There are two different methods of quantifying the *extrinsic* MI, namely the averaging method and the histogram based method [33]. The averaging method only relies on the *extrinsic*

LLRs and it quantifies the quality of the LLRs by assuming that the LLR magnitudes are truly proportional to the confidence that is warranted. By contrast, the histogram based method relies both on the *extrinsic* LLRs and on the correct bit values. Explicitly, the histogram based method does not trust the LLR values, but instead it quantifies their quality by comparing them to the correct bit values. If both the averaging method and histogram based method give similar MI, this implies that the LLRs are trustworthy and self-consistent, expressing neither too much nor too little confidence in the value of the corresponding bits. This typically leads to superior iterative decoding performance, as it will be explored in Section VI.
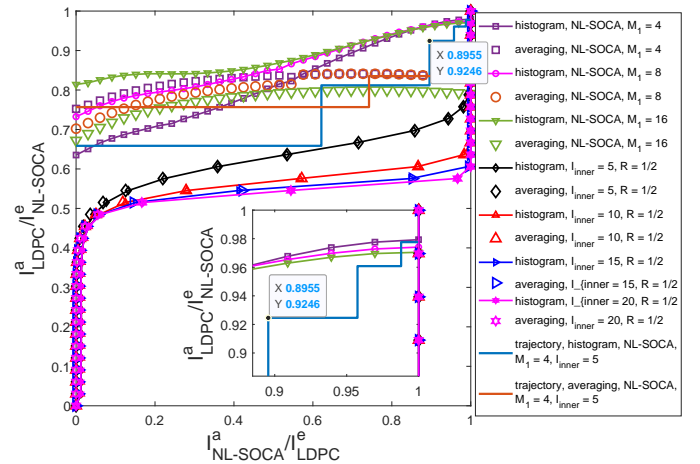

Fig. 6. NL-SOCA and LDPC EXIT functions of the LDPC-coded MMSE-IRC-NL-SOCA scheme, for the case of $N_{\mathrm{r}} = 4$ receive antennas, $N_{\mathrm{u}} = 4$ desired user transmit antennas, $N_{\mathrm{i}} = 1$ interfering user transmit antenna, $K' = 2048$ information bits, an LDPC coding rate of $R = 1/2$ using base graph 2, an SNR of 22 dB, an SIR of 0 dB, $N_{\mathrm{c}} = 64$ subcarriers, when using 16-QAM modulation for communication over a frequency selective fading channel with $L = 4$ channel taps. For the NL-SOCA tree search, the number of child nodes extended in each layer is $\boldsymbol{M} = [M_1\ 1\ 1\ 1]$ and the number of survivor child nodes retained in each layer is $\boldsymbol{K} = [M_1\ M_1\ M_1\ M_1]$, where $M_1 \in 4, 8, 16$.

Fig. 6 characterizes the EXIT functions of both the NL-SOCA detector and of the LDPC decoder in the proposed LDPC-coded MMSE-IRC-NL-SOCA scheme, for the case of $N_{\mathrm{r}} = 4$ RAs, $N_{\mathrm{u}} = 4$ desired user TAs, $N_{\mathrm{i}} = 1$ interfering

TABLE II
THEORETICAL COMPLEXITY OF DIFFERENT COMPONENTS IN THE MIMO-OFDM RECEIVER AS QUANTIFIED BY THE NUMBER OF ARITHMETIC OPERATIONS PERFORMED.

	MMSE-IRC	QAM soft demodulation	NL-SOCA $M_1 = 4$	NL-SOCA $M_1 = 8$	NL-SOCA $M_1 = 16$	LLR slicing	DL in the MMSE-IRC scheme	DL in the MMSE-IRC-NL-SOCA scheme	LDPC
additional /subtraction	190 464	568 320	3 709 952	6 200 320	11 033 600	-	114 688	393 216	991 952
compare	-	57 344	55 296	189 184	393 984	4 096	36 864	65 536	366 288
multiplication	366 592	812 032	5 862 400	8 303 616	12 983 296	-	114 688	393 216	-
real value division	-	8 192	87 040	152 576	278 528	-	-	-	-
complex value division	2 560	2 560	49 664	49 664	49 664	-	-	-	-
square root	-	-	2 048	2 048	2 048	-	-	-	-
exponential	-	-	425 984	819 200	1 605 632	-	-	-	175 968
logarithm	-	-	-	-	-	-	-	-	175 968

user TA, $K' = 2048$ information bits, an LDPC coding rate of $R = 1/2$ using the LDPC base graph 2 of [14], an SNR of 22 dB, an SIR of 0 dB, $N_c = 64$ subcarriers when employing 16-QAM modulation for communication over a frequency selective fading channel having $L = 4$ channel taps. For the NL-SOCA tree search of Fig. 3, the number of child nodes created in each layer is $\boldsymbol{M} = [M_1\ 1\ 1\ 1]$ and the number of survivor child nodes retained in each layer is $\boldsymbol{K} = [M_1\ M_1\ M_1\ M_1]$, where $M_1 \in 4, 8, 16$. As shown in Fig. 6, when the number of iterations I_{inner} performed within the LDPC decoder is increased, the LDPC EXIT function moves downwards, which represents improved LDPC decoding performance. However, only diminishing returns are seen upon exceeding $I_{\text{inner}} = 20$. Hence, upon considering the trade-off between the performance and complexity, $I_{\text{inner}} = 20$ may be recommended for LDPC decoding. As shown in Fig. 6, when the NL-SOCA parameter M_1 is increased, the *extrinsic* MIs measured by the histogram based method increase, which represents improved decoding performance, albeit at the cost of increased complexity as shown in Table. II. The trajectories between the LDPC EXIT function and NL-SOCA EXIT function present the iterative decoding processing between the LDPC decoder and NL-SOCA detector, and the number of staircases suggests the number of outer iterations. Considering the complexity of employing LDPC decoding one time is much lower than that of employing NL-SOCA detector one time, we prefer to increase the number of inner iterations in the LDPC decoding to reduce the number of outer iterations.

Observe in Fig. 6, the *extrinsic* MIs measured for the LDPC decoder using the averaging and histogram based methods match each other, indicating that the LDPC decoder produces self-consistent LLRs. By contrast, the SOCA EXIT functions obtained using the averaging and histogram methods do not match each other, which indicates that the clipped *extrinsic* LLRs of $\tilde{c}'^e$ are inconsistent as discussed above. This may be explained by the reduced complexity of the NL-SOCA detector, which leads to some over-confident or under-confident LLRs being generated. This motivates the use of the DL block shown in Fig. 3 in order to adjust the values of the *extrinsic* LLRs of $\tilde{c}'^e$, for making them more self-consistent and hence improving the iterative decoding performance.
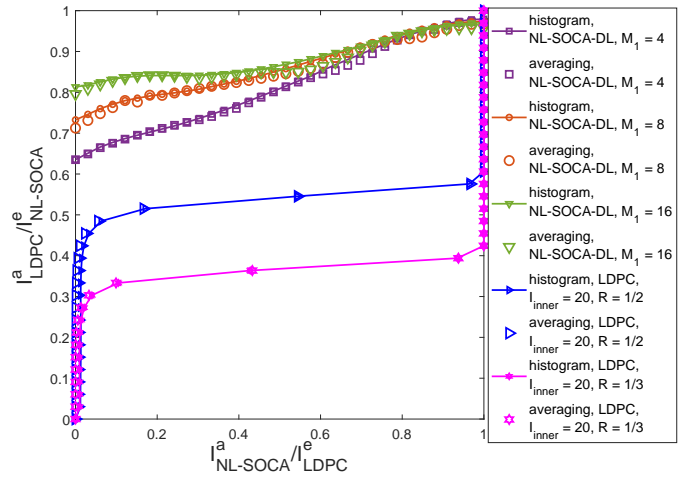

Fig. 7. NL-SOCA-DL and LDPC EXIT functions for the LDPC-coded MMSE-IRC-NL-SOCA-DL scheme for the case of $N_r = 4$ RAs, $N_u = 4$ desired user TAs, $N_i = 1$ interfering user TA, $K' = 2048$ information bits, base graph 2, an SNR of 22 dB, an SIR of 0 dB, $N_c = 64$ subcarriers when using 16-QAM modulation for communication over a frequency selective fading channel with $L = 4$ channel taps. In the NL-SOCA tree search, the number of extended child nodes in each layer $\boldsymbol{M} = [M_1\ 1\ 1\ 1]$ and the number of survived child nodes in each layer $\boldsymbol{K} = [M_1\ M_1\ M_1\ M_1]$.

Fig. 7 characterizes the NL-SOCA-DL EXIT function for various M_1 values in the LDPC coded MMSE-IRC-NL-SOCA-DL scheme, where DL is employed for correcting the inconsistent raw *extrinsic* LLRs of $\tilde{c}'^e$. Here, the *extrinsic* MIs $I^e_{\text{NL-SOCA}}$ are measured based on the corrected *extrinsic* LLRs of $\bar{c}^e$. Owing to the use of DL, the NL-SOCA EXIT functions obtained using the averaging method and histogram method can be seen to match each other in Fig. 7, which demonstrates that the corrected *extrinsic* LLRs of $\bar{c}^e$ are much more self-consistent than the raw *extrinsic* LLRs $\tilde{c}'^e$. Fig. 7 also characterizes the LDPC EXIT functions for a coding rate of $R = 1/3$ using both the averaging and the histogram based method. As before, the EXIT LDPC functions match well and move downward compared to the coding rate of $R = 1/2$ used in Fig. 6. This illustrates the superiority of LDPC decoding upon using a reduced coding rate [34]. However, this improved LDPC decoding is achieved at the cost of eroded spectral

N_r RAs	4
N_u TAs of the desired user	4
N_i TAs of the interfering user	1
K' information bits	2048
N_c subcarriers	64
L channel taps	4
BG	2
L_{max} clipping value	4

efficiency and increased complexity.

VI. SIMULATION RESULTS

In this section, we characterize the performance of the proposed MMSE-IRC-NL-SOCA, MMSE-IRC-NL-SOCA-DL, and MMSE-IRC-DL schemes, as well as the benchmarker MMSE-IRC scheme introduced in Section IV. Furthermore, we also compare the performance of the proposed schemes and of the benchmarker in different scenarios.
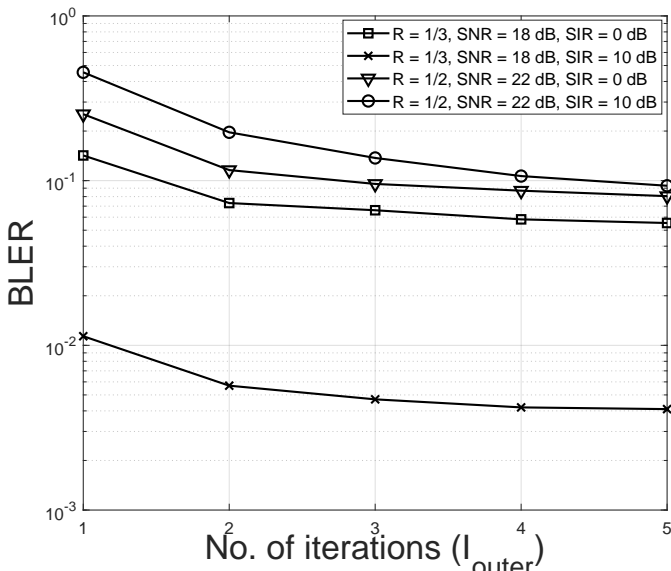
Fig. 8. BLER performance as a function of the number of iterations performed between the NL-SOCA detector and LDPC decoder in the MMSE-IRC-NL-SOCA scheme, for the case of $N_r = 4$ RAs, $N_u = 4$ user TAs, $N_i = 1$ interfering user TA, $K' = 2048$ information bits, $L_{max} = 4$ clipping value, BG $= 2$, $N_c = 64$ subcarriers when using 16-QAM modulation for communication over a frequency selective fading channel with $L = 4$ channel taps. In the NL-SOCA tree search, the number of child nodes created at each layer is $\boldsymbol{M} = [M_1\ 1\ 1\ 1]$ and the number of surviving child nodes in each layer is $\boldsymbol{K} = [M_1\ M_1\ M_1\ M_1]$. Plots are provided for various combinations of coding rates R, SNR, and SIR.

Table III characterizes the fundamental parameters used in the following investigations. Fig. 8 characterizes the BLER performance of the proposed MMSE-IRC-NL-SOCA scheme as a function of the number of iterations I_{outer} performed between the NL-SOCA detector and the LDPC decoder for different coding rates R, SNR, and SIR when using a NL-SOCA parameter value of $M_1 = 4$. As seen in Fig. 8, the decoding performance benefits from increasing the number of iterations I_{outer} performed between the NL-SOCA detector and LDPC decoder, although the BLER improvement becomes

insignificant when I_{outer} is larger than 4. Motivated by this, we adopt $I_{outer} = 4$ iterations between the NL-SOCA detector and LDPC decoder in the following investigations.
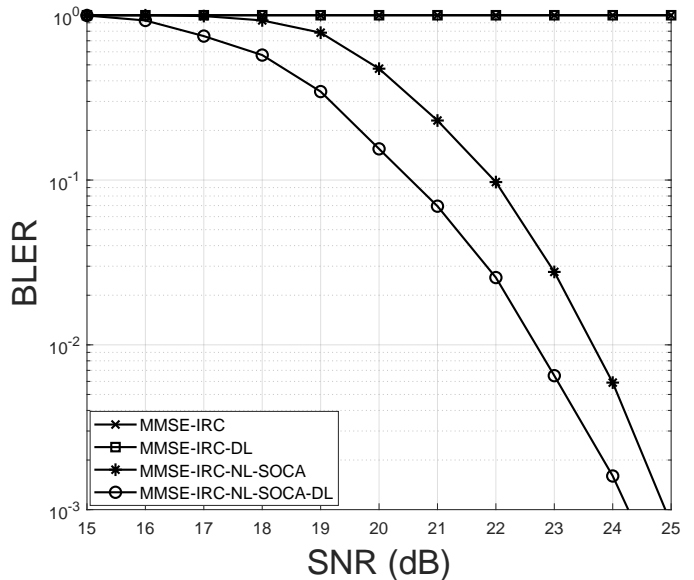

Fig. 9. BLER performance as a function of SNR for various schemes, for the case of $N_r = 4$ RAs, $N_u = 4$ user TAs, $N_i = 1$ interfering user TA, $K' = 2048$ information bits, $L_{max} = 4$ slicing value, coding rate $R = 1/2$, SIR $= 0$ dB, BG $= 2$, $N_c = 64$ subcarriers, when using 16-QAM modulation for communication over a frequency selective fading channel with $L = 4$ channel taps. For the NL-SOCA tree search in the case of the MMSE-IRC-NL-SOCA and MMSE-IRC-NL-SOCA-DL schemes, the number of child nodes created at each layer is $\boldsymbol{M} = [4\ 1\ 1\ 1]$ and the number of surviving child nodes in each layer is $\boldsymbol{K} = [4\ 4\ 4\ 4]$. The number of outer iterations performed between the NL-SOCA detector and LDPC decoder is $I_{outer} = 4$.

The following simulation results characterize different comparisons of our proposed schemes with the benchmarkers. Fig. 9 highlight the scenario of using a high coding rate R and a low SIR. Fig. 10 portrays the case of using a high coding rate R and a high SIR, while Fig. 11 characterizes the case of using a low coding rate R and a low SIR. Then, Fig. 12 features the case of using a low coding rate R and a high SIR.

Fig. 9 highlights a particular problem encountered for a rate of $R = 1/2$ at a low SIR of 0 dB. Explicitly, the MMSE-IRC benchmarker may fail to detect the transmitted signal $\mathbf{X}_1$, regardless of the SNR. In this case, the DL module is unable to improve the capability of the MMSE-IRC scheme to detect the transmitted signal $\mathbf{X}_1$, hence the MMSE-IRC-DL scheme characterizing Fig. 9 offers the same poor performance as the MMSE-IRC scheme. However, in this case, our proposed MMSE-IRC-NL-SOCA scheme benefits from combining linear MMSE-IRC detection with NL-SOCA detection in order to overcome the effect of the interference and achieve successful decoding. Furthermore, Fig. 9 shows that the 'DL' module of Fig. 1 used for correcting the sliced *extrinsic* LLRs $\tilde{c}'^e$ may improve the decoding performance by around 0.6 dB at a BLER of 10^{-3}, when the number of child nodes extended in each layer is $\boldsymbol{M} = [4\ 1\ 1\ 1]$ and the number of surviving child nodes in each layer is $\boldsymbol{K} = [4\ 4\ 4\ 4]$. In this case, the complexity of the MMSE-IRC-NL-SOCA-DL scheme is about 2% higher than that of the MMSE-IRC-NL-
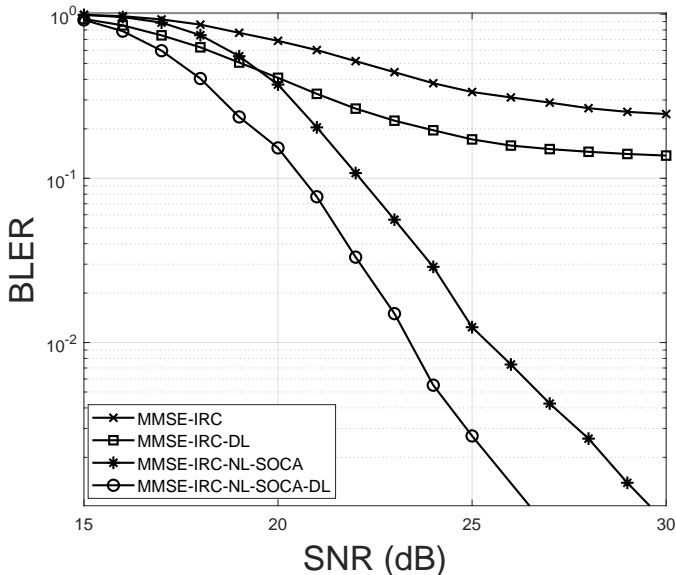
SOCA scheme, as detailed in Section IV.

Fig. 10. BLER performance as a function of SNR for various schemes, for the case of $N_{\mathrm{r}} = 4$ RAs, $N_{\mathrm{u}} = 4$ user TAs, $N_{\mathrm{i}} = 1$ interfering user TA, $K' = 2048$ information bits, $L_{\max} = 4$ slicing value, coding rate $R = 1/2$, SIR $= 10$ dB, BG $= 2$, $N_{\mathrm{c}} = 64$ subcarriers when using 16-QAM modulation for communication over a frequency selective fading channel with $L = 4$ channel taps. For the NL-SOCA tree search in the case of MMSE-IRC-NL-SOCA and MMSE-IRC-NL-SOCA-DL schemes, the number of child nodes created in each layer is $\boldsymbol{M} = [4\ 1\ 1\ 1]$ and the number of surviving child nodes in each layer is $\boldsymbol{K} = [4\ 4\ 4\ 4]$. The number of outer iterations performed between the NL-SOCA detector and LDPC decoder is $I_{\mathrm{outer}} = 4$.

Fig. 10 characterizes the BLER performance of both the proposed schemes and of the benchmarkers, upon increasing the SIR to 10 dB, when using a coding rate of $R = 1/2$. In this case, the MMSE-IRC scheme may be seen to successfully detect the transmitted signals, albeit with an error floor. Moreover, compared to the MMSE-IRC benchmaker, the DL module of the MMSE-IRC-DL scheme may be seen to reduce the error floor, but fails to completely eliminate it. By contrast, our proposed MMSE-IRC-NL-SOCA scheme does eliminate the error floor of the MMSE-IRC scheme, and the DL module of the MMSE-IRC-NL-SOCA-DL scheme further improves the decoding performance by about 3 dB at a BLER of 10^{-3}, while only increasing the complexity by about 2%.

Fig. 11 characterizes the case of using a low coding rate of $R = 1/3$ and a low SIR of 0 dB. When the coding rate is low, the MMSE-IRC scheme becomes capable of successful decoding, hence eliminating the error floor, even when the SIR is low. The MMSE-IRC scheme performs better than the MMSE-IRC-NL-SOCA scheme at low SNRs. This may be explained by the observation that at low SNRs, the NL-SOCA module is unable to make reliable decisions, and therefore outputs incorrect signals. By contrast, the MMSE-IRC scheme works on the basis of noisy versions of the correct signals. At low SNRs, this noise is preferable to the errors introduced by the NL-SOCA module. By contrast, at high SNRs, the NL-SOCA module makes reliable decisions, and therefore outputs the correct signals. Therefore, the proposed MMSE-IRC-NL-SOCA scheme becomes capable of outperforming the benchmarker at high SNRs. More specifically, it obtains about
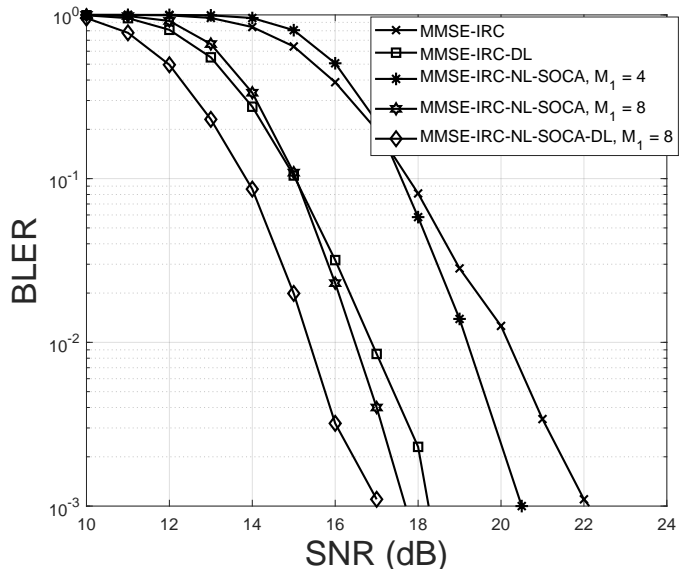

Fig. 11. BLER performance as a function of SNR for various schemes, for the case of $N_{\mathrm{r}} = 4$ RAs, $N_{\mathrm{u}} = 4$ user TAs, $N_{\mathrm{i}} = 1$ interfering user TA, $K' = 2048$ information bits, $L_{\max} = 4$ slicing value, coding rate $R = 1/3$, SIR $= 0$ dB, BG $= 2$, $N_{\mathrm{c}} = 64$ subcarriers, when using 16-QAM modulation for communication over a frequency selective fading channel with $L = 4$ channel taps. For the NL-SOCA tree search in the case of the MMSE-IRC-NL-SOCA and MMSE-IRC-NL-SOCA-DL schemes, the number of child nodes created in each layer is $\boldsymbol{M} = [M_1\ 1\ 1\ 1]$ and the number of surviving child nodes in each layer is $\boldsymbol{K} = [M_1\ M_1\ M_1\ M_1]$, where $M_1 = 4$ and 8 are considered. The number of outer iterations performed between the NL-SOCA detector and LDPC decoder is $I_{\mathrm{outer}} = 4$.

1.5 dB gain at a BLER of 10^{-3} compared to the MMSE-IRC benchmarker, albeit at the cost of increasing the complexity by a factor of four, when $M_1 = 4$. However, as a benefit of using DL, the MMSE-IRC-DL benchmarker offers about 1.75 dB gain, compared to the proposed MMSE-IRC-NL-SOCA scheme using $M_1 = 4$. Additionally, the decoding performance of the proposed MMSE-IRC-NL-SOCA scheme can be significantly improved by increasing the value of M_1 to 8, offering around 2.5 dB gain at a BLER of 10^{-3} over the MMSE-IRC-NL-SOCA using $M_1 = 4$. Furthermore, the DL module can further improve the performance by about 0.65 dB at a BLER of 10^{-3} compared to the MMSE-IRC-NL-SOCA scheme using $M_1 = 8$. Observe that, the MMSE-IRC-NL-SOCA-DL scheme achieves about 1.25 dB gain at a BLER of 10^{-3} and $M_1 = 8$, compared to the MMSE-IRC-DL scheme. However, it may also be seen that upon using the higher M_1 value of 8, the performance improvement achieved by employing DL in the MMSE-IRC-NL-SOCA-DL scheme becomes modest, compared to the MMSE-IRC-NL-SOCA scheme. But again, the complexity of the MMSE-IRC-NL-SOCA-DL scheme is about 4.6 times higher than that of the MMSE-IRC-DL scheme when $M_1 = 8$.

Fig. 12 characterizes the case of using a low coding rate of $R = 1/3$ and a high SIR of 10 dB. In this case, the MMSE-IRC benchmarker offers better performance than the proposed MMSE-IRC-NL-SOCA scheme when $M_1 = 4$. Upon increasing M_1 to 8, the performance of the proposed MMSE-IRC-NL-SOCA scheme becomes better than that of the MMSE-IRC scheme. However, the MMSE-IRC-DL bench-
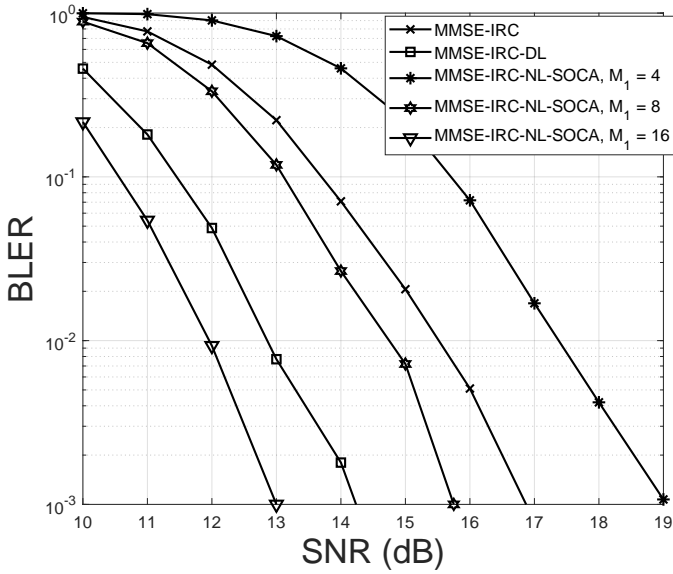
Fig. 12. BLER performance as a function of SNR for various schemes, for the case of $N_r = 4$ RAs, $N_u = 4$ user TAs, $N_i = 1$ interfering user TA, $K' = 2048$ information bits, $L_{max} = 4$ clipping value, coding rate $R = 1/3$, SIR = 10 dB, BG = 2, $N_c = 64$ subcarriers, when using 16-QAM modulation for communication over a frequency selective fading channel with $L = 4$ channel taps. For the NL-SOCA tree search in the case of the MMSE-IRC-NL-SOCA scheme, the number of child nodes created in each layer is $\boldsymbol{M} = [M_1 \ 1 \ 1 \ 1]$ and the number of surviving child nodes in each layer is $\boldsymbol{K} = [M_1 \ M_1 \ M_1 \ M_1]$, where $M_1 = 4, 8$ and 16 are considered. The number of outer iterations performed between the NL-SOCA detector and LDPC decoder is $I_{outer} = 4$.

Fig. 13. Throughput as a function of the SNR where a BLER of 10^{-1} is achieved, for the case of $N_r = 4$ RAs, $N_u = 4$ user TAs, $N_i = 1$ interfering user TA, $K' = 2048$ information bits, $L_{max} = 4$ slicing value, SIR = 0 dB, BG = 2, $N_c = 64$ subcarriers, when using 16-QAM modulation for communication over a frequency selective fading channel with $L = 4$ channel taps. For the NL-SOCA tree search in the case of the MMSE-IRC-NL-SOCA scheme, the number of child nodes created in each layer is $\boldsymbol{M} = [M_1 \ 1 \ 1 \ 1]$ and the number of surviving child nodes in each layer is $\boldsymbol{K} = [M_1 \ M_1 \ M_1 \ M_1]$, where $M_1 = 4, 8$ and 16 are considered. The number of outer iterations performed between the NL-SOCA detector and LDPC decoder is $I_{outer} = 4$.

marker benefits from the LLR correction advocated and offers about 1.5 dB gain at a BLER of 10^{-3}, compared to the MMSE-IRC-NL-SOCA scheme when $M_1 = 8$. In this case, the complexity of the MMSE-IRC-DL scheme is as low as about 18% of that of the MMSE-IRC-NL-SOCA scheme. We may obtain about 1.25 dB gain by further increasing M_1 to 16 in the MMSE-IRC-NL-SOCA, compared to the MMSE-IRC-DL scheme. However, in this case, the complexity of the MMSE-IRC-NL-SOCA scheme is about 6.8 times higher than that of the MMSE-IRC-DL scheme. We may conclude that the combination of the MMSE-IRC and SOCA is not motivated, when the coding rate is low and the SIR is high.

The findings of the BLER plots inferred from Fig. 9 to Fig. 12 may be summarized by the throughput VS. SNR plots. Fig. 13 characterizes the throughput as a function of the SNR, where a BLER of 10^{-1} is achieved for SIR of 0 dB, while Fig. 14 characterizes the case of an SIR of 10 dB. The effective throughput of the system may be calculated as $R \log_2(G)$, which implies that the higher coding rates R and higher modulation orders G lead to higher throughputs [34]. The throughput plots of Fig. 13 and Fig. 14 are obtained by simulating a variety of different LDPC coding rates and in each case, identifying the SNR where the BLER becomes 10^{-1}. Then, we plotted $R \log_2(G)$ against that SNR.

As seen in Fig. 13 and Fig.14, when the throughput is higher than $4/3$, the proposed MMSE-IRC-NL-SOCA scheme using $M_1 = 4$ offers better performance than the MMSE-IRC benchmarker. However, when the throughput is lower than $4/3$, the MMSE-IRC benchmarker offers better perfor-
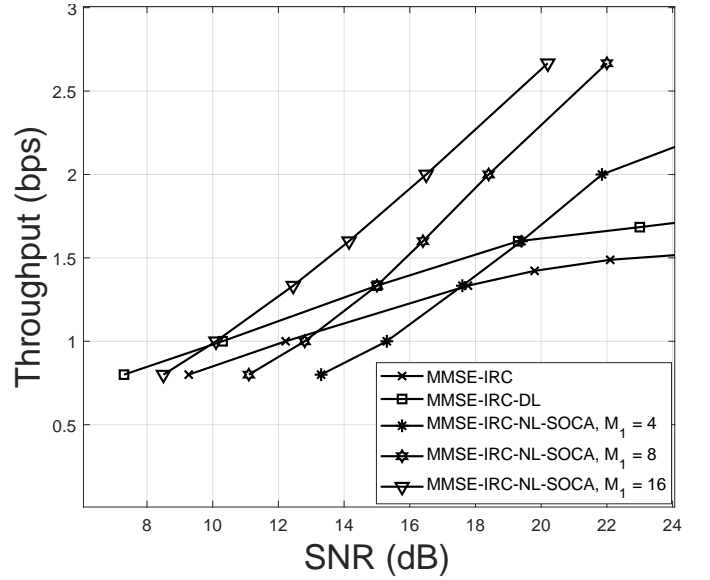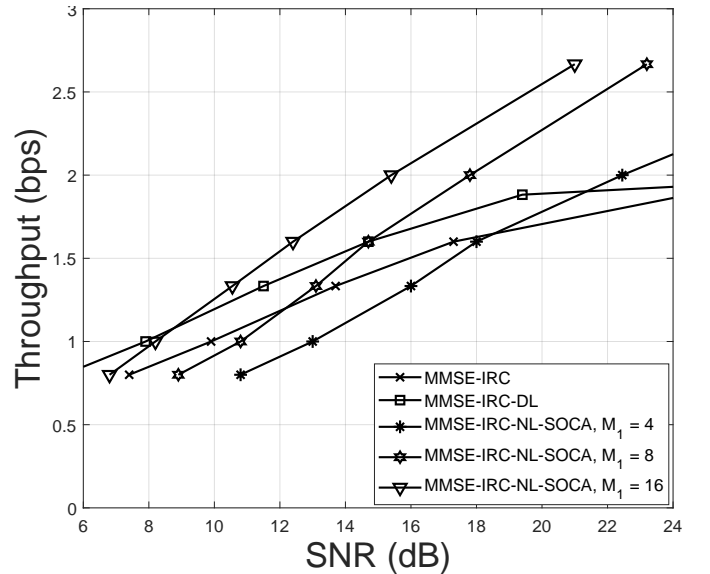

Fig. 14. Throughput as a function of the SNR where a BLER of 10^{-1} is achieved, for the case of $N_r = 4$ RAs, $N_u = 4$ user TA, $N_i = 1$ interfering user TA, $K' = 2048$ information bits, $L_{max} = 4$ slicing value, SIR = 10 dB, BG = 2, $N_c = 64$ subcarriers, when using 16-QAM modulation for communication over a frequency selective fading channel with $L = 4$ channel taps. For the NL-SOCA tree search in the case of the MMSE-IRC-NL-SOCA scheme, the number of child nodes created in each layer is $\boldsymbol{M} = [M_1 \ 1 \ 1 \ 1]$ and the number of surviving child nodes in each layer is $\boldsymbol{K} = [M_1 \ M_1 \ M_1 \ M_1]$, where $M_1 = 4, 8$ and 16 are considered. The number of outer iterations performed between the NL-SOCA detector and LDPC decoder is $I_{outer} = 4$.

mance. This may be explained by the observation that at a low throughput, the proposed MMSE-IRC-NL-SOCA scheme exhibits a degraded performance, particularly when M_1 is small. However, the performance of the proposed MMSE-IRC-NL-SOCA scheme may be improved at a low throughput by increasing the value of M_1, so that it outperforms the MMSE-IRC benchmarker even for throughput as low as $4/5$. However, Fig. 13 and Fig. 14 show that the addition of DL to the MMSE-IRC benchmarker in the MMSE-IRC-DL scheme offers better performance than the MMSE-IRC-NL-SOCA scheme using $M_1 = 16$, when throughput is lower than 1. This is notable, because the complexity of the MMSE-IRC-DL scheme is much lower than that of the proposed MMSE-IRC-NL-SOCA scheme. However, Fig. 13 and Fig. 14 show that both the MMSE-IRC and the MMSE-IRC-DL schemes have error floors upon increasing the SNR, which prevents the throughput from exceeding 1.9 in the case of SIR = 10 dB. Indeed, as shown in Fig. 9, when the coding rate R is high and the SIR is low, the MMSE-IRC scheme fails to detect the transmitted signals, and the addition of the DL module is unable to reverse this situation either. Compared to Fig. 13, Fig. 14 shows that even when the SIR is increased to 10 dB, both the MMSE-IRC and MMSE-IRC-DL scheme still suffer from error floors at high throughputs. In these cases, the SNR required to achieve a BLER of 10^{-1} extends towards infinity. By contrast, the proposed MMSE-IRC-NL-SOCA scheme avoids error floors at high throughputs, and it offers a significant advantage compared to the MMSE-IRC benchmarkers. Therefore, the proposed MMSE-IRC-NL-SOCA scheme may be set to support higher-throughput communication in MIMO-OFDM systems suffering from high interference. Furthermore, the DL module can improve the performance of the MMSE-IRC scheme.

Based on the results discussed in this section, we may conclude that the proposed MMSE-IRC scheme is the preferred option in the case of higher-throughput schemes for MIMO-OFDM systems operating in the face of high interference. However, the MMSE-IRC-DL scheme may be recommended when the throughput is low, considering that it has a lower complexity than the MMSE-IRC-NL-SOCA-DL scheme when $M_1 = 8$. Explicitly, it has about five times lower complexity.

VII. CONCLUSIONS

The MMSE-IRC equalizer was reformulated, in order to make it compatible with nonlinear detectors. This has the benefit of significantly enhancing the maximum achievable throughput in interference-constrained scenarios, while mitigating the error floor of the MMSE-IRC schemes at high throughputs. We proposed a specific design example, in which we concatenate a MMSE-IRC equalizer with a NL SOCA detector in a LDPC-MIMO-OFDM system. Furthermore, we proposed the use of a DL module for improving the self-consistency of the LLRs entered into the low-complexity SOCA detector, in order to further improve its decoding performance. The benefit of this approach is demonstrated using EXIT charts, in order to characterize the self-consistency of the LLRs proposed by the SOCA detector both with and without

the DL module of Fig. 1. Our BLER results of Fig. 9 and Fig. 10 show that when high-throughput operation is required using a high LDPC coding rate, the MMSE-IRC scheme may exhibit error floors and fail to detect the transmitted signals, when the interference power is high. In this case, the proposed MMSE-IRC-NL-SOCA scheme is shown to eliminate these error floors and successfully decode the transmitted signals, where the DL module may also be employed for further improving the performance of the proposed MMSE-IRC-NL-SOCA scheme. The proposed MMSE-IRC-NL-SOCA scheme obtains about 1.5 dB gain at the cost of a four-fold complexity. Using the DL technique, we demonstrate a 3 dB improvement for the MMSE-IRC-NL-SOCA-DL scheme at the cost of increasing the complexity by a modest factor of 1.02, compared to the proposed MMSE-IRC-NL-SOCA scheme.

REFERENCES

[1] L. Hanzo, Y. Akhtman, L. Wang, and M. Jiang, *MIMO-OFDM for LTE, WiFi and WiMAX: Coherent versus non-coherent and cooperative turbo transceivers*. John Wiley & Sons, 2010, vol. 9.

[2] L. Hua, Y. Wang, Z. Lian, Y. Su, and Z. Xie, "LADMM-based PAPR-aware precoding for massive MIMO-OFDM downlink systems," *IEEE Transactions on Vehicular Technology*, vol. 72, no. 1, pp. 735–746, 2023.

[3] O. W. G. 4, "7-2x UL performance improvement (ULPI) work item WG4-2022-01," 2022.

[4] A. M. Kuzminskiy, Y. I. Abramovich, P. Xiao, R. Tafazolli, and J. Huang, "Maximum likelihood optimization of adaptive asynchronous interference mitigation beamformer," *IEEE Transactions on Signal Processing*, vol. 69, pp. 5134–5146, 2021.

[5] A. Hakimi, S. Zargari, C. Tellambura, and S. Herath, "Sum rate maximization of MIMO monostatic backscatter networks by suppressing residual self-interference," *IEEE Transactions on Communications*, vol. 71, no. 1, pp. 512–526, 2023.

[6] Z. Wu, S. Zhu, J. Xu, L. Lan, and M. Zhang, "Interference suppression method with MR-FDA-MIMO radar," *IEEE Transactions on Aerospace and Electronic Systems*, pp. 1–15, 2023.

[7] N.-D. Dao, J. Soler-Garrido, R. Cepeda, Y. Sun, and W. H. Chin, "Design and evaluation of antenna selection methods for interference rejection combining," *IEEE Transactions on Wireless Communications*, vol. 11, no. 8, pp. 2751–2759, 2012.

[8] X. Ji, M. Jin, W. Liu, and Z. Xu, "Inter-cell interference suppression for MIMO-OFDM systems based on complex-valued neural network," in *2020 IEEE International Conference on Communications Workshops (ICC Workshops)*, 2020, pp. 1–6.

[9] Y. Ohwatari, N. Miki, Y. Sagae, and Y. Okumura, "Investigation on interference rejection combining receiver for space–frequency block code transmit diversity in LTE-advanced downlink," *IEEE Transactions on Vehicular Technology*, vol. 63, no. 1, pp. 191–203, 2014.

[10] S. Moon, H. Choe, M. Chu, C. You, H. Liu, J.-H. Kim, J. Kim, D. Kim, and I. Hwang, "Advanced receiver for interference suppression and cancellation in sidelink system of LTE-advanced," *Wireless Personal Communications*, vol. 95, pp. 4321–4335, 2017.

[11] S. Moon, H. Choe, M. Chu, C. You, H. Liu, J.-H. Kim, J. Kim, D. J. Kim, and I. Hwang, "Design and performance analysis of soft decision-based network-assisted interference cancellation and suppression scheme," *Wireless Personal Communications*, vol. 96, no. 4, pp. 5849–5863, 2017.

[12] P. Karunakaran, T. Wagner, A. Scherb, and W. Gerstacker, "On interference rejection combining for LTE-a systems: Analysis of covariance estimators and an iterative algorithm for frequency-selective channels," in *2015 IEEE 81st Vehicular Technology Conference (VTC Spring)*, 2015, pp. 1–5.

[13] R. Makkar, V. Kotha, M. Sheeba Kumari, D. Rawal, V. K. Chakka, and N. Kumar, "Performance of downlink SISO NR system using MMSE-IRC receiver," in *2020 IEEE 3rd 5G World Forum (5GWF)*, 2020, pp. 619–624.

[14] G. RP-201118, "Views on Rel-17 NR demodulation requirements," *Intel Corporation*, 07 2020.

[15] R. M. de Amorim, J. Wigard, I. Z. Kovacs, T. B. Sorensen, and P. E. Mogensen, "Enabling cellular communication for aerial vehicles: Providing reliability for future applications," *IEEE Vehicular Technology Magazine*, vol. 15, no. 2, pp. 129–135, 2020.

[16] Y. Yuan, Z. Yuan, and L. Tian, "5G non-orthogonal multiple access study in 3GPP," *IEEE Communications Magazine*, vol. 58, no. 7, pp. 90–96, 2020.

[17] F. Liu, H. Zhao, X. Quan, Y. Liu, and Y. Tang, "Eigen domain interference rejection combining algorithm for MIMO systems," *IEEE Communications Letters*, vol. 20, no. 5, pp. 850–853, 2016.

[18] J. Yin, W. Ge, X. Han, B. Liu, and L. Guo, "Partial FFT demodulation with IRC in MIMO-SC-FDE communication over Doppler distorted underwater acoustic channels," *IEEE Communications Letters*, vol. 23, no. 11, pp. 2086–2090, 2019.

[19] C.-C. Cheng, S. Sezginer, H. Sari, and Y. T. Su, "Linear interference suppression with covariance mismatches in MIMO-OFDM systems," *IEEE Transactions on Wireless Communications*, vol. 13, no. 12, pp. 7086–7097, 2014.

[20] D. L. Milliner, E. Zimmermann, J. R. Barry, and G. Fettweis, "A fixed-complexity smart candidate adding algorithm for soft-output MIMO detection," *IEEE Journal of Selected Topics in Signal Processing*, vol. 3, no. 6, pp. 1016–1025, 2009.

[21] J. Chen, T.-Y. Wang, J.-Y. Wu, C.-P. Li, S. X. Ng, R. G. Maunder, and L. Hanzo, "Deep learning aided llr correction improves the performance of iterative mimo receivers," *IEEE Transactions on Vehicular Technology*, pp. 1–15, 2023.

[22] S. Shao, P. Hailes, T.-Y. Wang, J.-Y. Wu, R. G. Maunder, B. M. Al-Hashimi, and L. Hanzo, "Survey of turbo, LDPC, and polar decoder ASIC implementations," *IEEE Communications Surveys & Tutorials*, vol. 21, no. 3, pp. 2309–2333, 2019.

[23] C. Studer and H. Bölcskei, "Soft–input soft–output single tree-search sphere decoding," *IEEE Transactions on Information Theory*, vol. 56, no. 10, pp. 4827–4842, 2010.

[24] Y. Xin, S. A. Mujtaba, T. Zhang, and J. Jiang, "Bypass decoding: A reduced-complexity decoding technique for LDPC-coded MIMO-OFDM systems," *IEEE Transactions on Vehicular Technology*, vol. 57, no. 4, pp. 2319–2333, 2008.

[25] S. Roger, A. Gonzalez, V. Almenar, and G. Matz, "An efficient fixed-complexity sphere decoder with quantized soft outputs," *IEEE Communications Letters*, vol. 16, no. 11, pp. 1828–1831, 2012.

[26] G. Papa, D. Ciuonzo, G. Romano, and P. Salvo Rossi, "A dominance-based soft-input soft-output MIMO detector with near-optimal performance," *IEEE Transactions on Communications*, vol. 62, no. 12, pp. 4320–4335, 2014.

[27] R. H. Gohary and T. J. Willink, "On LLR clipping in BICM-IDD non-coherent MIMO communications," *IEEE Communications Letters*, vol. 15, no. 6, pp. 650–652, 2011.

[28] M. Mohammadkarimi, M. Mehrabi, M. Ardakani, and Y. Jing, "Deep Learning-Based Sphere Decoding," *IEEE Transactions on Wireless Communications*, vol. 18, no. 9, pp. 4368–4378, 2019.

[29] S. Papaharalabos and F. Lazarakis, "Approximated Box-Plus decoding of LDPC codes," *IEEE Communications Letters*, vol. 19, no. 12, pp. 2074–2077, 2015.

[30] Y. S. Cho, J. Kim, W. Y. Yang, and C. G. Kang, *MIMO-OFDM wireless communications with MATLAB.* John Wiley & Sons, 2010.

[31] K.-L. Chung and W.-M. Yan, "The complex Householder transform," *IEEE Transactions on Signal Processing*, vol. 45, no. 9, pp. 2374–2376, 1997.

[32] A. Irturk, B. Benson, A. Arfaee, and R. Kastner, "Automatic generation of decomposition based matrix inversion architectures," in *2008 International Conference on Field-Programmable Technology*, 2008, pp. 373–376.

[33] M. El-Hajjar and L. Hanzo, "EXIT charts for system design and analysis," *IEEE Communications Surveys & Tutorials*, vol. 16, no. 1, pp. 127–153, 2014.

[34] T. Richardson and S. Kudekar, "Design of low-density parity check codes for 5G New Radio," *IEEE Communications Magazine*, vol. 56, no. 3, pp. 28–34, 2018.